

# End-to-end 2D-3D Registration between Image and LiDAR Point Cloud for Vehicle Localization

Guangming Wang, Yu Zheng, Yanfeng Guo, Zhe Liu, Yixiang Zhu, Wolfram Burgard, and Hesheng Wang

**Abstract**—Robot localization using a previously built map is essential for a variety of tasks including highly accurate navigation and mobile manipulation. A popular approach to robot localization is based on image-to-point cloud registration, which combines illumination-invariant LiDAR-based mapping with economical image-based localization. However, the recent works for image-to-point cloud registration either divide the registration into separate modules or project the point cloud to the depth image to register the RGB and depth images. In this paper, we present I2PNet, a novel end-to-end 2D-3D registration network. I2PNet directly registers the raw 3D point cloud with the 2D RGB image using differential modules with a unique target. The 2D-3D cost volume module for differential 2D-3D association is proposed to bridge feature extraction and pose regression. 2D-3D cost volume module implicitly constructs the soft point-to-pixel correspondence on the intrinsic-independent normalized plane of the pinhole camera model. Moreover, we introduce an outlier mask prediction module to filter the outliers in the 2D-3D association before pose regression. Furthermore, we propose the coarse-to-fine 2D-3D registration architecture to increase localization accuracy. We conduct extensive localization experiments on the KITTI Odometry and nuScenes datasets. The results demonstrate that I2PNet outperforms the state-of-the-art by a large margin. In addition, I2PNet has a higher efficiency than the previous works and can perform the localization in real-time. Moreover, we extend the application of I2PNet to the camera-LiDAR online calibration and demonstrate that I2PNet outperforms recent approaches on the online calibration task.

**Index Terms**—Vehicle localization, image-to-point cloud registration, cost volume module.

## I. INTRODUCTION

**H**IGH-ACCURACY robot localization in pre-built maps is an essential task for autonomous mobile robots, since robot localization is the foundation of various tasks, such as high-accuracy robot navigation and mobile manipulation. Recently, most researches focus on same-modality mapping and localization, including Light Detection And Ranging (LiDAR) point cloud-based mapping and localization, and image-based

\*This work was supported in part by the Natural Science Foundation of China under Grant U1613218 and 61722309. The first three authors contributed equally. Corresponding Author: Hesheng Wang.

G. Wang, and H. Wang are with the Department of Automation, Shanghai Jiao Tong University, Shanghai 200240, China and Key Laboratory of System Control and Information Processing, Ministry of Education of China.

Y. Zheng is with the Department of Artificial Intelligence, Shanghai Jiao Tong University, Shanghai 200240, China.

Y. Guo is with Electrical and Computer Engineering at University of California, Los Angeles, the United States.

Z. Liu is with the Institute of Artificial Intelligence, Shanghai Jiao Tong University, Shanghai 200240, China.

Y. Zhu is with the Department of Electrical Engineering, Shanghai Jiao Tong University, Shanghai 200240, China.

W. Burgard is with the Department of Engineering, University of Technology Nuremberg, Germany.

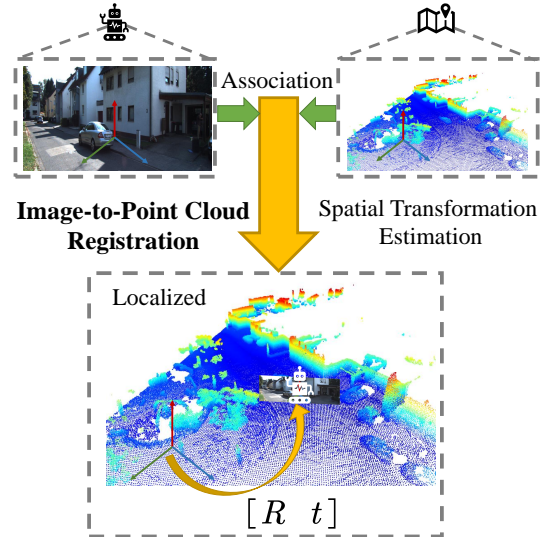


Figure 1. This figure shows the pipeline of the image-to-point cloud registration-based monocular camera localization in LiDAR point cloud map. Image-to-point cloud registration associates the image and point cloud and estimates the spatial transformation between them. With the estimated transformation, the pose of the monocular camera in the LiDAR map is obtained. Therefore, the robot is localized in the global map coordinate system.

mapping and localization. The LiDAR point cloud-based mapping and localization can reach considerable localization accuracy with the place recognition and point cloud-to-point cloud registration [1]–[6]. However, this localization method requires the mobile robot equipped with the expensive LiDAR, which greatly limits the popularity of mobile robots. Meanwhile, the accuracy of image-based mapping and localization [7]–[11] is greatly limited by poor illumination and featureless environments. In contrast to same-modality mapping and localization, with cross-modality mapping and localization, i.e., LiDAR point cloud-based mapping and monocular camera image-based localization, the robot to be localized is only required to be equipped with the economical monocular camera. Additionally, the LiDAR point cloud-based mapping is invariant to the illumination and environment features and can represent the 3D scenes with high accuracy. Therefore, cross-modality mapping and localization are more promising than same-modality mapping and localization and worthy to research.

The conventional monocular camera localization in the pre-built LiDAR point cloud map adopts the matching between the camera image and synthetic image from LiDAR map [12], [13], or registration between LiDAR map and local 3D point cloud reconstruction from the image sequence [14]. However, synthetic image rendering is costly. In addition, the 3D local reconstruction requires image sequence input and can fail in

featureless scenes. Therefore, image-to-point cloud registration, which directly registers the image and LiDAR point cloud as shown in Fig. 1, is more suitable for monocular camera localization in the pre-built LiDAR point cloud map. However, image-to-point cloud registration is more complex than same-modality registration due to the different characteristics of the different modalities. The RGB image contains rich texture information which the LiDAR point cloud lacks, while the LiDAR point cloud contains rich 3D geometric information which the RGB image lacks. Therefore, image-to-point cloud registration for vehicle localization starts to be widely researched after the occurrence of brain-inspired [15] Deep Neural Networks (DNNs). Most DNN-based image-to-point cloud registration methods for vehicle localization divide the image-to-point cloud registration into separate modules [16]–[21]. DNN-based methods can improve the performance of a part of the modules, such as image-to-point cloud association [16]–[19]. However, the separate modules are designed or optimized for separate targets. The error of the former modules will not be corrected in the subsequent modules since they are not jointly optimized for the unique target. In addition, several works [16]–[19], [21] adopt the Random SAmple Consensus (RANSAC) [22] based Perspective-n-Point (PnP) solvers [23], [24] or non-linear optimization solvers [25] as one of the separate modules. These iterative modules limit the efficiency of these methods. Recently, several works [26]–[28] attempt to register the image with point cloud in an end-to-end manner. However, these works project the raw point cloud into a depth image, utilize Convolutional Neural Networks (CNNs) to associate the RGB image and depth image, and finally regress the spatial transformation. The projection of the point cloud limits the application of these methods to small-range localization, since a great number of points lose during the projection when the misalignment between the point cloud and the image is large.

In this paper, we introduce I2PNet, a novel end-to-end image-to-point cloud registration method for vehicle localization. In contrast to recent methods, I2PNet is a fully end-to-end architecture without separate modules and directly associates the 2D RGB image and the raw 3D LiDAR point cloud. Therefore, I2PNet is an end-to-end 2D-3D registration method between image and LiDAR point cloud. To realize end-to-end 2D-3D registration, three challenges need to be overcome: 1) Since the 3D coordinates of LiDAR points are contiguous but the 2D coordinates of the image pixels are discrete, a LiDAR point can hardly find a precisely corresponding pixel; 2) To make the model not limited by a specific camera, the image-to-point cloud association should be independent of the camera intrinsic; 3) Since the LiDAR point cloud fully covers the surrounding area while the image only covers the front area, many point-to-pixel associations are outliers and should be automatically filtered in a differential manner. For the first two challenges, we propose a novel differential 2D-3D association module, named 2D-3D cost volume module. Specifically, we solve the first challenge by generating point-wise features of implicit point-to-pixel correspondences in the 2D-3D cost volume module and enabling all the points to be softly associated with the pixels. Notably, the position information of the points and pixels is embedded in the

correspondence features since the geometric information is essential for the transformation estimation. For the second challenge, the 2D-3D cost volume estimation is performed on the normalized plane of the pinhole camera model since the coordinates on the normalized plane are naturally independent of the camera intrinsic. Through the above designs, the 2D-3D cost volume module can generate the point-wise 2D-3D cost volumes to present the 2D-3D association differentially. For the third challenge, an outlier mask prediction module is proposed. In this module, the 2D-3D cost volumes and LiDAR point features are utilized to generate outlier masks. For more accurate outlier filtering, the context point-to-pixel implicit correspondence features are gathered to embed the local spatial transformation information in the 2D-3D cost volumes. The geometric transformation information improves the outlier prediction and results in better registration. Finally, the 2D-3D cost volumes are masked by the outlier masks and aggregated to estimate the global spatial transformation between the point cloud and the image. In addition, we propose a coarse-to-fine 2D-3D registration architecture and perform fine registration based on the coarse prior knowledge. The coarse registration results are used to warp the point cloud to gain a pair of the image and point cloud with smaller misalignment for the fine registration. Furthermore, the coarse cost volumes and outlier masks are fused with the fine cost volumes and outlier masks respectively to gain a better spatial transformation estimation.

In summary, our main contributions are:

- We introduce a novel end-to-end 2D-3D registration architecture for vehicle localization. Different from existing methods, all the modules in our architecture are jointly optimized by a unique target, and the complete 3D point cloud is preserved for large-range localization.
- We propose the novel 2D-3D cost volume module and outlier mask prediction module to enable end-to-end 2D-3D registration. 2D-3D cost volume module differentially associates 3D points and 2D pixels on the camera intrinsic-independent space, while outlier mask prediction module enables outlier filtering and ensures robust pose regression.
- The coarse-to-fine 2D-3D registration is purposed, which utilizes the coarse prior knowledge to refine the registration and improve localization accuracy.
- We conduct extensive robot localization experiments on multiple datasets [29], [30] and various localization ranges to show the superiority and generalization of I2PNet. Moreover, we evaluate the efficiency of I2PNet and demonstrate the end-to-end pipeline can improve both performance and efficiency.
- We extend the application of I2PNet to the camera-LiDAR online calibration and demonstrate the effectiveness of I2PNet on various tasks.

## II. RELATED WORK

In this section, we will introduce the state-of-the-art image-to-point cloud registration works for robot localization and the recent coarse-to-fine architectures, followed by a review of state-of-the-art camera-LiDAR online calibration methods.

### A. Image-to-Point Cloud Registration for Robot Localization

2D3D-MatchNet [16] is one of the earliest works focusing on image-to-point cloud registration for robot localization. The 2D and 3D keypoints are obtained by SIFT and ISS [31] respectively. Then, a neural network with three branches is introduced to learn the descriptors for keypoints. Finally, EPnP [24] is adopted to estimate the transformation between the image and the point cloud with the 2D-3D correspondences. DeepI2P [19] splits the image-to-point cloud registration problem into a classification problem and an optimization problem. A cross-modality neural network is adopted to classify whether the points fall into the image frustum. The classification results are utilized to construct the cost function of the inverse camera projection. The optimization solver solves the transformation that minimizes the value of the cost function. CorrI2P [18] designs a cross-modality network to extract the image-to-point cloud overlapping region and corresponding dense descriptors for the image and point cloud. CorrI2P constructs dense image-to-point cloud correspondences and uses iterative RANSAC-based EPnP [24] to estimate the relative pose. EFGHNet [20] adopts the divide-and-conquer strategy to divide the image-to-point cloud registration into four separate sub-networks. These sub-networks are responsible for the horizon and ground normal alignments, rotation estimation, and translation estimation. The four sub-networks are sequentially applied and the subsequent networks depend on the results of the previous networks.

These methods divide the image-to-point cloud registration into separate modules for large-range robot localization. The separation makes the modules separately optimized and thus not able to refine the error of the previous modules.

*In I2PNet, all parts are differentially united and jointly optimized, which enables the error refinement of the subsequent modules and makes the registration more robust.*

### B. Coarse-to-Fine Architecture

The coarse-to-fine architecture is first introduced in the optical flow approaches [32], [33]. These methods are based on simple image pyramids. PWC-Net [34] first introduces the coarse-to-fine architecture based on image feature pyramids and obtains great performance in optical flow estimation. The Pyramid, Warping, and Cost Volume (PWC) structure estimates the optical flow from coarse-grained features to fine-grained features and performs flow refinement based on the coarse cost volume and flow estimation. The PWC structure has been adopted in other areas including scene flow estimation [35]–[37] and deep LiDAR odometry [38] from point clouds, etc.

A few recent works [26]–[28] attempt to form an end-to-end image-to-point cloud registration network for robot localization with the 2D-2D coarse-to-fine architecture. CMRNet [26] is one of the representative methods. CMRNet projects the point cloud as a depth image. Based on the depth image, it utilizes the CNN-based PWC-Net [34] to perform the 2D-2D coarse-to-fine registration between the RGB and depth images. CMRNet shows the effectiveness of the 2D-2D coarse-to-fine architecture in small-range localization. However, depth image projection limits the application of CMRNet to large-range localization.

*In contrast to these 2D-2D coarse-to-fine registration methods, we construct the 2D-3D coarse-to-fine registration architecture between image and point cloud, which makes I2PNet is effective for large-range localization.*

### C. Camera-LiDAR Online Calibration

The camera-LiDAR online calibration task is to online correct the calibration error between the camera and LiDAR. The conventional camera-LiDAR online calibration methods extract the common low-level features of the image and point cloud, such as contours [39], [40] or intensity [41], and match the features. They utilize feature matches to construct the cost function and optimize the cost function to gain the decalibration matrix. The first deep-learning-based online camera-LiDAR calibration method is RegNet [42]. It utilizes several Network-In-Network (NIN) blocks [43] to extract the features of the RGB image and depth map to obtain image features and depth features respectively. The extracted image features and depth features are simply concatenated and fed into several NIN blocks and Fully Connected (FC) layers to perform feature matching and pose regression respectively. The subsequent works of RegNet focus on better loss to improve the calibration. CalibNet [44] introduces the photometric loss and point cloud distance losses to perform the geometrical supervision. In addition, RGGNet [45] introduces the geodesic distance loss to supervise the calibration in  $se(3)$  space based on the Riemannian geometry and the tolerance regularizer loss to supervise the error bound with an implicit tolerance model.

The recent DNN-based camera-LiDAR calibration mostly adopts the depth image representation of the LiDAR point cloud and utilizes CNNs to realize the image-to-point cloud registration like CMRNet. Therefore, their application is limited in the online calibration task where the misalignment between the image and point cloud is small.

*The 2D-3D registration architecture of our I2PNet is suitable for both robot localization and online calibration. Moreover, I2PNet outperforms the recent online calibration methods.*

## III. END-TO-END 2D-3D REGISTRATION

### A. Network Architecture

Image-to-point cloud registration is defined as that given the RGB image and the point cloud, the network estimates the spatial transformation between the image and the point cloud. I2PNet performs end-to-end 2D-3D image-to-point cloud registration with three main components: feature extraction, coarse registration, and fine registration. The main architecture of I2PNet is shown in Fig. 2.

In the feature extraction, the image and point cloud feature pyramids extract the hierarchical image and point features for the image-to-point cloud association.

In the coarse registration, the 2D-3D cost volume module associates the image and point cloud in the third layer of the pyramid and outputs the 2D-3D cost volumes. The context gathering module further aggregates the 2D-3D cost volumes. Then, the outlier masks are predicted from the 2D-3D cost volumes. The outlier masks are used to mask the 2D-3D cost volumes for the outlier filtering and pose regression.

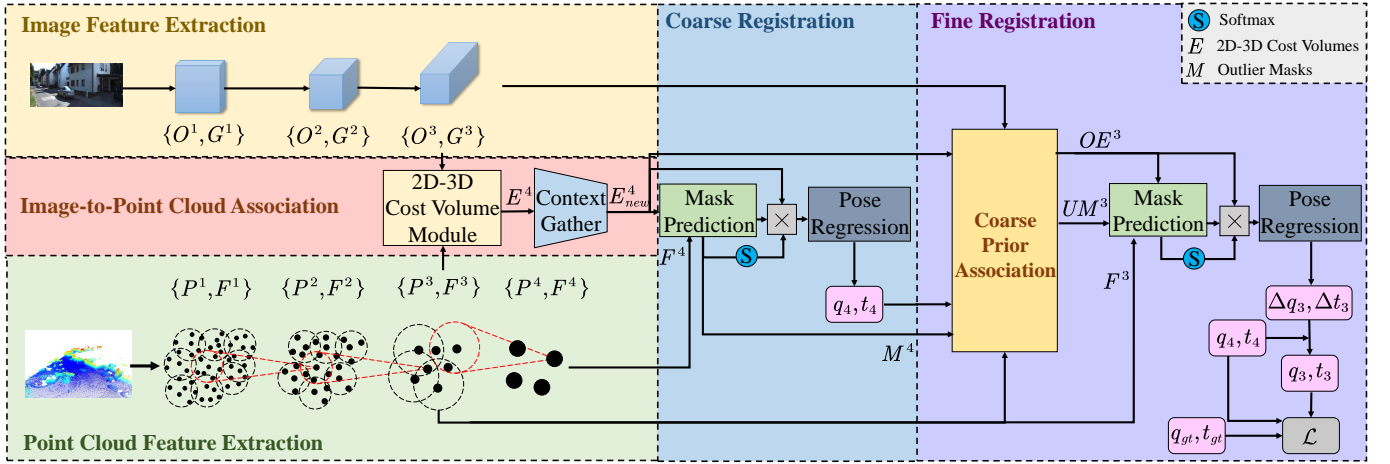


Figure 2. The outline of I2PNet. I2PNet takes the RGB image and the raw LiDAR point cloud as input. Through the feature extraction pyramid, coarse registration, and fine registration, the network finally predicts relative pose between the image and point cloud. The detailed structure of coarse prior association is shown in Fig. 3.

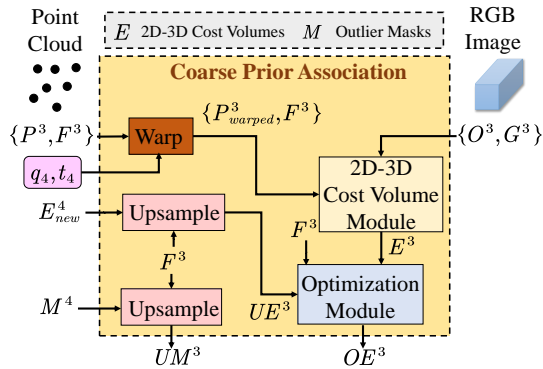


Figure 3. The detailed structure of the coarse prior association in Fig. 2.

In the fine registration, as shown in Fig. 3, we perform the coarse prior association to transfer the prior knowledge from the coarse registration to the fine registration. In coarse prior association, the 2D-3D cost volumes and outlier masks from the coarse registration are firstly upsampled. Then, the coarse relative pose is used to warp the point cloud. After the warping, the warped point cloud and the image are associated to generate the 2D-3D cost volumes of the residual spatial transformation. The 2D-3D cost volumes of the residual spatial transformation are fused with the upsampled coarse 2D-3D cost volumes in the optimization module to output the optimized 2D-3D cost volumes.

The subsequent modules in fine registration estimate the residual transformation based on the results of coarse prior association. Concretely, the fine outlier masks are predicted using the optimized 2D-3D cost volumes. After fine outlier mask prediction, the predicted fine outlier masks are fused with the upsampled coarse outlier masks to gain the optimized outlier masks. The optimized 2D-3D cost volumes are masked by the optimized outlier mask. The residual relative pose is regressed from the masked 2D-3D cost volumes. Finally, the coarse relative pose is multiplied by the residual relative pose, and the fine relative pose is obtained.

We optimize the end-to-end registration network by minimizing the composition of relative pose losses in the coarse and fine registrations.

## B. Feature Extraction

1) *Image Feature Extraction*: The features of the input RGB image are extracted by three layers. Each layer consists of 5 convolutional blocks. Each convolutional block is the composition of  $3 \times 3$  convolution, batch normalization, leaky Rectified-Linear Unit (ReLU), and max-pooling. Max-pooling is adopted to downsample the image to different resolutions. The extracted image features in the  $l$ -th layer are  $G^l = \{g_i^l | i = 1, 2, \dots, M^l\}$ , in which  $M^l$  is the number of pixels. The 2D coordinates of the pixels on the pixel plane are represented by the position information  $O^l = \{o_i^l | i = 1, 2, \dots, M^l\}$ .

2) *Point Cloud Feature Extraction*: The features of the input point cloud are extracted by PointNet++ [46]. PointNet++ adopts Farthest Point Sampling (FPS) to select an evenly distributed subset of the original point cloud. Each point in the selected subset is treated as the center point of a point group. For each center point, several points are grouped by querying the nearest neighbors from all the points in the point cloud. The features of each point group are aggregated by PointNet [47]. However, because of the high time complexity of FPS and neighborhood query among all the points, the vanilla PointNet++ is inefficient for the large-scale point cloud from the LiDAR point cloud map. Therefore, we refer to EfficientLO-Net [48] to use the stride-based sampling and projection-aware grouping to replace the sampling and neighborhood query methods in PointNet++. To apply the stride-based sampling and projection-aware grouping, the 2D spherical coordinates  $(u_s, v_s)$  of each point are calculated as [49]:

$$\begin{pmatrix} u_s \\ v_s \end{pmatrix} = \begin{pmatrix} \frac{1}{2} [1 - \arctan(y, x) \cdot \pi^{-1}] \cdot W \\ [1 - (\arcsin(z/r) + f_{up}) \cdot f^{-1}] \cdot H \end{pmatrix}, \quad (1)$$

in which  $(x, y, z)$  are the 3D coordinates of each point, and  $r = \sqrt{x^2 + y^2 + z^2}$  is the range of each point.  $f = f_{up} + f_{down}$  is the vertical field-of-view of the LiDAR sensor, in which  $f_{up}$  and  $f_{down}$  are the up and down vertical field-of-view respectively.  $H$  and  $W$  are the initial upper bounds of the 2D spherical coordinates, i.e.,  $0 \leq u_s < W$  and  $0 \leq v_s < H$ . Based on the 2D spherical coordinates, stride-based sampling can perform efficient sampling to obtain the center points. The

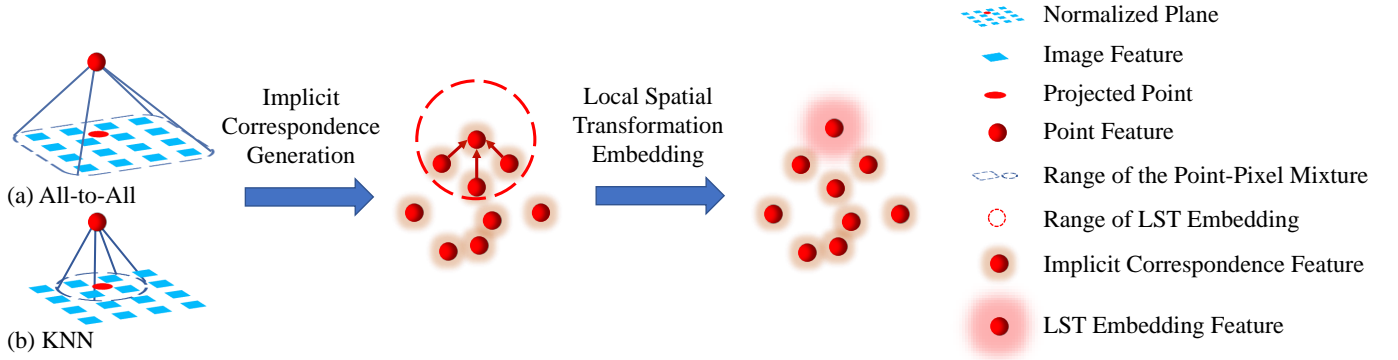


Figure 4. The process diagram of the 2D-3D cost volume module. The implicit correspondence (IC) generation module uses an all-to-all or KNN-based point-pixel mixture to match the points and pixels on the normalized plane of the pinhole camera model. Then, the similarities of each point-pixel pair are calculated and aggregated to generate the point-wise IC features. Based on the IC features, the local spatial transformation (LST) embedding module aggregates the IC features of the neighbors of each point to estimate the LST information and embeds it in the LST embedding features. The module finally outputs the LST embedding features as the 2D-3D cost volumes.

stride-based sampling refers to the stride mechanism of the 2D convolution. The points whose 2D coordinates are exactly integral multiples of the strides are sampled as the center points. After obtaining the center points, projection-aware grouping performs the efficient neighborhood query by reducing the search space of the 3D nearest neighbors. A fixed-size 2D kernel whose center is the 2D coordinates of each sampled center point is adopted for the searching space reduction. The searching space is reduced from the whole point to the kernel points whose 2D coordinates are inside the fixed-size 2D kernel. Due to the characteristic of spherical projection, the 3D nearest neighbors are included in the kernel points when selecting an appropriate kernel size [48]. Therefore, the 3D nearest neighbors are queried from the kernel points through the KNN algorithm. It is noticed that the points whose distances towards the center point are over the distance threshold will not be selected by KNN. By stride-based sampling and projection-aware grouping, I2PNet can efficiently extract features of the large-scale raw point cloud.

The point features from fine-grained to coarse-grained are extracted by four layers in point cloud feature extraction. In the  $l$ -th layer,  $P^l = \{p_i^l | i = 1, 2, \dots, N^l\}$  represent the position information, and  $F^l = \{f_i^l | i = 1, 2, \dots, N^l\}$  represent the point features, where  $N^l$  is the number of the points. Notably,  $P^0$  are the coordinates of the input point cloud while  $F^0$  are the initial point features. The feature extraction is as follows:

$$f_i^l = \text{MaxPool}(\text{MLP}(\{f_{i,k}^{l-1}\}_{k=1}^{K^l})), \quad (2)$$

where  $K^l$  is the number of points in a point group. *MaxPool* means max-pooling operation. *MLP* means the shared MLP block. In addition, the position information of the next layer is obtained as  $P^l = \mathcal{S}(P^{l-1})$ , where  $\mathcal{S}$  is the sampling method.

### C. 2D-3D Cost Volume Module

1) *Overview*: As shown in Fig. 4, the 2D-3D cost volume module consists of two components, the implicit correspondence (IC) generation module and the local spatial transformation (LST) embedding module.

IC generation module calculates the feature similarities of the point-pixel pairs and generates the IC features of each

point according to the similarities. Notably, we generate the point-wise IC features rather than pixel-wise IC features, since the 6-DoF relative pose should be regressed from the features of points in 3D space rather than pixels on 2D plane. As shown in Fig. 4, two different types of point-pixel mixtures are proposed to generate the point-pixel pairs. The first is the all-to-all point-pixel mixture, which selects all the pixels to form the point-pixel pairs. The second is the  $K$  Nearest Neighbors (KNN)-based point-pixel mixture, which selects the nearest pixel neighbors towards each point on the normalized plane of the pinhole camera model to form the point-pixel pairs. The appropriate type of point-pixel mixture is chosen according to the initial misalignment between the image and the point cloud. For the task whose initial misalignment is large, the KNN-based mixture can not find the correspondence. Therefore, the all-to-all mixture is adopted for the coarse registration, while the KNN-based mixture is adopted for the fine registration. For the task whose initial misalignment is small, the KNN-based mixture is adopted in both the coarse and fine registrations for the finer correspondence generation. Moreover, the image and point position information is embedded in the IC features for spatial transformation estimation in the subsequent modules.

In the following LST embedding module, the IC features are further gathered to embed the local spatial transformation in LST embedding features for the outlier mask prediction module. The LST embedding features are the results of the differential 2D-3D association, which are denoted as the 2D-3D cost volumes

2) *Detailed Pipeline*: We present the detailed pipeline of the 2D-3D cost volume module in Fig. 5. In the implicit correspondence generation module, the point cloud and image are projected and inverse-projected respectively onto the camera intrinsic-independent space, i.e., the normalized plane of the camera pinhole model. The point cloud is projected as:

$$\begin{bmatrix} \bar{x}_i \\ \bar{y}_i \\ 1 \end{bmatrix}^T = \frac{1}{z_i} \begin{bmatrix} x_i \\ y_i \\ z_i \end{bmatrix}^T, \quad (3)$$

where  $p_i = (x_i, y_i, z_i)^T$  are the 3D coordinates of the  $i$ -th point, and  $\bar{p}_i = (\bar{x}_i, \bar{y}_i, 1)^T$  are the coordinates on the normalized

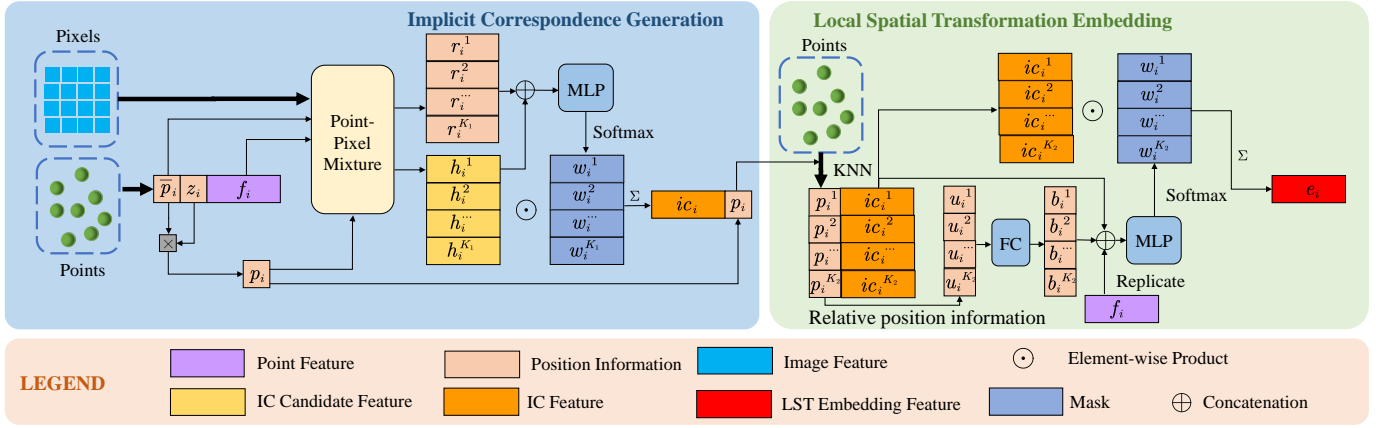


Figure 5. The detailed pipeline of the 2D-3D cost volume module. Given the features of the image and point cloud, as well as their position information, the module estimates the LST embedding features as the 2D-3D cost volumes. The detailed structures of the point-pixel mixtures are shown in Fig. 6 and Fig. 7.

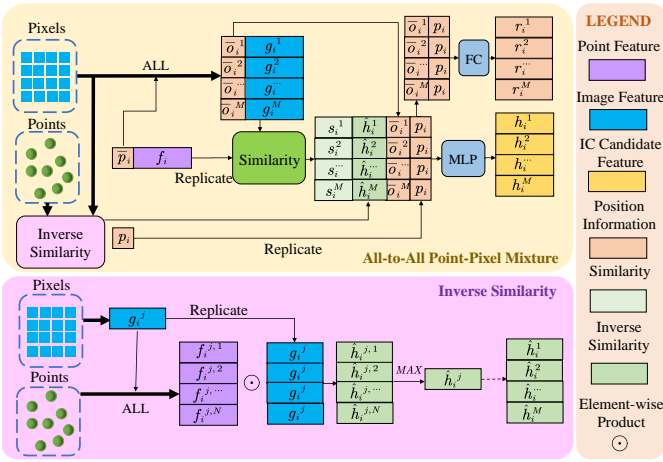


Figure 6. The all-to-all point-pixel mixture for the coarse registration. The all-to-all mixture treats all the pixels as the correspondence candidates of the point. In addition, the inverse similarity is adopted for robust correspondence generation.

plane. In addition, the image is inverse-projected as:

$$\begin{bmatrix} \bar{u} \\ \bar{v} \\ 1 \end{bmatrix}^T = K_c^{-1} \begin{bmatrix} u \\ v \\ 1 \end{bmatrix}^T, \quad (4)$$

where  $K_c$  is the intrinsic matrix of the camera, while  $(u, v)^T$  is the 2D coordinates  $o_i$  of the  $i$ -th pixel on the pixel plane, and  $(\bar{u}, \bar{v}, 1)^T$  are the coordinates on the normalized plane which is represented by  $\bar{o}_i$ . After the projection and inverse projection, both points and pixels are on the normalized plane. Their coordinates  $\bar{o}_i$  and  $\bar{p}_i$  are independent of the intrinsic. Then, the point-pixel mixture is performed to generate the point-pixel pairs. For the all-to-all point-pixel mixture, as shown in Fig. 6, all the pixels are selected as the matching candidates for the  $i$ -th point. The position information and image features of the pixel candidates are  $\{\bar{o}_i^k\}_{k=1}^M$  and  $\{g_i^k\}_{k=1}^M$  respectively. For the KNN-based point-pixel mixture, as shown in Fig. 7,  $K$  nearest pixel neighbors on the normalized plane are selected for each point  $\bar{p}_i$  through KNN.  $\{\bar{o}_i^k\}_{k=1}^K$  and  $\{g_i^k\}_{k=1}^K$  represent the position information and image features of the  $K$  nearest pixels respectively. Then, the similarity between  $f_i$  and  $g_i^k$  are calculated for the implicit correspondence generation. The

similarity is calculated as the element-wise product of the normalized feature vectors. The formula is:

$$s_i^k = \frac{f_i - \mu(f_i)}{\sigma(f_i)} \odot \frac{g_i^k - \mu(g_i^k)}{\sigma(g_i^k)}, \quad (5)$$

where  $s_i^k$  is the similarity between the features of the  $k$ -th pixel candidate and its center point.  $\odot$  is the element-wise production.  $\mu(f_i)$  and  $\sigma(f_i)$  are the mean and standard deviation of the point feature vector  $f_i$ , while  $\mu(g_i^k)$  and  $\sigma(g_i^k)$  are the mean and standard deviation of the image feature vector  $g_i^k$ . In addition, for the all-to-all mixture, the single-direction similarity from point to pixel can be influenced by the spatial similarity of image features, which can result in the wrong implicit correspondences. Therefore, inspired by [37], we utilize the inverse similarity for the all-to-all pattern to make the IC generation more reliable. The inverse similarity is the maximal pixel-to-point similarity among all the pixels. Specifically, for the  $i$ -th point, the  $j$ -th pixel candidate selects all the points as the inverse matching candidates. The point features of the inverse candidates are  $\{f_i^{j,l}\}_{l=1}^N$ . Then, the inverse similarity  $\hat{h}_i^j$  of the  $j$ -th pixel candidate is calculated by:

$$\hat{h}_i^j = \text{MaxPool}(\{f_i^{j,l} \odot g_i^j\}_{l=1}^N). \quad (6)$$

Based on the inverse similarity, only the point-pixel pair that has high similarities in both the forward and inverse directions can be as the correct correspondence.

The IC candidate features  $\{h_i^k\}_{k=1}^{K_1}$  between the  $i$ -th point and its  $k$ -th pixel candidate are generated as the Eq. 7 for the all-to-all pattern and Eq. 8 for the KNN pattern respectively.  $K_1$  is the number of pixel candidates of each point, which is  $M$  for the all-to-all mixture or  $K$  for the KNN-based mixture. The equations of IC candidate feature generation are:

$$h_i^k = \text{MLP}(s_i^k \oplus \hat{h}_i^k \oplus \bar{o}_i^k \oplus p_i), \quad (7)$$

$$h_i^k = \text{MLP}(s_i^k \oplus \bar{o}_i^k \oplus p_i), \quad (8)$$

where  $\oplus$  represents the concatenating operation.

The next step is to estimate the mask  $w_i^k$ , which is the correspondence salience of the  $k$ -th IC candidate feature for the  $i$ -th point. The formula is:

$$w_i^k = \text{Softmax}(\text{MLP}(h_i^k \oplus r_i^k)), \quad (9)$$

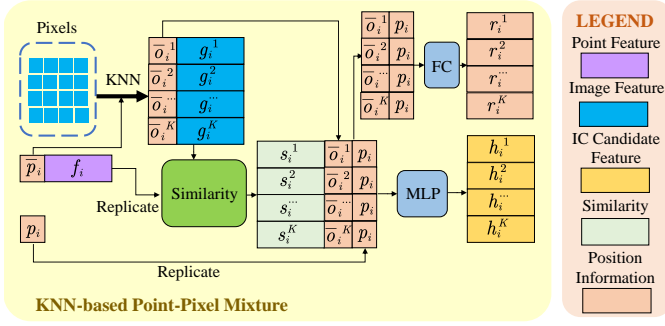


Figure 7. The KNN-based point-pixel mixture. This type of point-pixel mixture treats the  $K$  nearest pixel neighbors as the pixel correspondence candidates.

where  $r_i^k = FC(p_i \oplus \bar{o}_i^k)$  is the position embedding, and  $FC$  is the fully connected layer to further encode the position information. In addition, *Softmax* is adopted to normalize the saliencies. Then, the weighted sum of IC candidate features with the correspondence saliency is performed to generate the IC feature  $ic_i$  for the  $i$ -th point, as follows:

$$ic_i = \sum_{k=1}^{K_1} (h_i^k \odot w_i^k). \quad (10)$$

The weighted sum makes each point softly match the pixel candidates and resolves the challenge of precise explicit correspondence estimation.

After gaining the point-wise IC features, the local spatial transformation can be embedded. In the LST embedding module, the projection-aware grouping-based neighborhood query is adopted to query each point's  $K_2$  nearest point neighbors. The position information  $\{p_i^m\}_{m=1}^{K_2}$  and the IC features  $\{ic_i^m\}_{m=1}^{K_2}$  of the point neighbors are gathered. In addition, inspired by RandLA-Net [50], the relative position information between each point neighbor and its center point is calculated to enrich the position information. The overall position information  $\{u_i^m\}_{m=1}^{K_2}$  are composed of four parts: The absolute coordinates of the center point, the absolute coordinates of point neighbors, the relative coordinates, and the Euclidean distance, as follows:

$$u_i^m = p_i \oplus p_i^m \oplus (p_i^m - p_i) \oplus \|p_i^m - p_i\|, \quad (11)$$

where  $\|\cdot\|$  represents the  $L_2$ -norm. The overall position information is fed into an FC layer to obtain the position embedding  $b_i^m$  as follows:

$$b_i^m = FC(u_i^m). \quad (12)$$

Then, the weighted LST estimation is performed. The point feature  $f_i$  of the  $i$ -th center point, the position embedding  $b_i^m$  of the  $m$ -th point neighbor, and the IC feature  $ic_i^m$  of the  $m$ -th point neighbor are concatenated and fed into a shared MLP block to calculate the weights:

$$w_i^m = \text{Softmax}(MLP(f_i \oplus b_i^m \oplus ic_i^m)), \quad (13)$$

where  $w_i^m$  is the weight of the  $m$ -th point neighbor's IC feature for the  $i$ -th center point. Based on the estimated weights,

the weighted sum of the IC features is performed to estimate the local spatial transformation, as follows:

$$e_i = \sum_{m=1}^{K_2} (ic_i^m \odot w_i^m), \quad (14)$$

where  $e_i$  is the LST embedding features of the  $i$ -th point. Therefore,  $N$  LST embedding features are obtained as the 2D-3D cost volumes, which are represented by  $E = \{e_i | i = 1, 2, \dots, N\}$ . Specifically,  $E^4$  represents the 2D-3D cost volumes estimated in the coarse registration, and  $E^3$  represents the 2D-3D cost volumes estimated in the fine registration.

#### D. Coarse Registration

1) *Context Gathering Module*: To localize the robot within a large range, the context gathering module further gathers the 2D-3D cost volumes for the coarse registration. The 2D-3D association information in the context is utilized to refine the 2D-3D cost volume of each point.

Specifically, we use the same feature extraction module in the point cloud feature extraction to gather the 2D-3D cost volumes  $E^4$ . The gathered 2D-3D cost volumes are  $E_{new}^4 = \{e_{new,i}^4 | i = 1, 2, \dots, N^4\}$ , which is calculated as:

$$e_{new,i}^4 = \text{MaxPool}(MLP(\{e_{i,k}^4\}_{k=1}^{K^4})), \quad (15)$$

where the center points of each point group are sampled using the same indexes as the fourth layer of the point cloud feature extraction.

2) *Outlier Mask Prediction Module*: The 2D-3D cost volumes  $E_{new}^4$  embed the information of the 2D-3D association. However, the outliers of the 2D-3D association, such as the points out of the image frustum [19] which have no pixel correspondence, should be filtered. The former works [16], [18] utilize the RANSAC to filter the outliers for relative pose estimation. In this paper, the outlier masks are learned to filter the outliers based on the point features and LST embedding features.

In detail, in the coarse registration, the outlier mask prediction module uses the point features of the fourth layer  $F^4 = \{f_i^4 | i = 1, 2, \dots, N^4\}$  and context-gathered 2D-3D cost volumes  $E_{new}^4$  to estimate the coarse outlier masks  $M^4 = \{m_i^4 | i = 1, 2, \dots, N^4\}$ . The formula is:

$$m_i^4 = MLP(e_{i,new}^4 \oplus f_i^4). \quad (16)$$

3) *Pose Regression*: The pose regression first aggregates the 2D-3D cost volumes weighted by the outlier masks to generate the global spatial transformation embedding feature. Then, the FC layers decode the global spatial transformation embedding feature and obtain the relative pose between the image and point cloud. Specifically, the weighted sum of the 2D-3D cost volumes is adopted to aggregate the cost volumes. The weights  $MW^4 = \{mw_i^4\}_{i=1}^{N^4}$  are calculated by performing softmax on the outlier masks  $M^4$ . The outlier masks assign outliers with low weights. Thus, the inlier 2D-3D cost volumes are mainly aggregated. As for relative pose decoding, a middle layer with dropout operation is adopted during the training to overcome overfitting. In detail, an FC layer is first adopted to perform

the linear transformation on the global spatial transformation embedding feature to gain the middle feature. Then, the dropout operation is performed on the middle feature. Finally, the predicted quaternion  $q$  and the translation vector  $t$  are obtained by the linear transformation of two FC layers respectively on the middle feature. The predicted quaternion and translation vector in the coarse registration are denoted as  $q_4$  and  $t_4$ . The formula of the pose regression is:

$$q_4 = \frac{FC(\sum_{i=1}^{N^4} (e_{new,i}^4 \odot mw_i^4))}{|FC(\sum_{i=1}^{N^4} (e_{new,i}^4 \odot mw_i^4))|}, \quad (17)$$

$$t_4 = FC(\sum_{i=1}^{N^4} (e_{new,i}^4 \odot mw_i^4)), \quad (18)$$

where the quaternion is normalized to gain a unique representation of the rotation.

### E. Fine Registration

1) *Upsampling Layer*: In the fine registration, two upsampling layers are adopted to upsample the coarse 2D-3D cost volumes  $E_{new}^4$  and outlier masks  $M^4$  respectively. The upsampling converts the prior knowledge of coarse registration. In the upsampling layers, the projection-aware grouping-based neighborhood query is adopted to group  $K$  nearest points  $\{p_{i,k}^4\}_{k=1}^K$  from the point cloud  $P^4$  for each point  $p_i^3$  in the point cloud  $P^3$ . After querying, the relative position between each grouped point and its center point is calculated. Then, the coarse features of grouped points are concatenated with the relative position. The concatenated features are aggregated by a shared MLP block and a max-pooling operation. After the aggregation, the aggregated features and the point features  $F^3$  are concatenated and fed into an FC layer. Finally, the upsampled 2D-3D cost volumes  $UE^3 = \{ue_i^3 | i = 1, 2, \dots, N^3\}$  and outlier masks  $UM^3 = \{um_i^3 | i = 1, 2, \dots, N^3\}$  are outputted by the two upsampling layers respectively. The formulas are:

$$ue_i^3 = FC(f_i^3 \oplus \text{MaxPool}(MLP(\{e_{new,i,k}^4 \oplus (p_{i,k}^4 - p_i^3)\}_{k=1}^K))), \quad (19)$$

$$um_i^3 = FC(f_i^3 \oplus \text{MaxPool}(MLP(\{m_{i,k}^4 \oplus (p_{i,k}^4 - p_i^3)\}_{k=1}^K))). \quad (20)$$

$UE^3$  and  $UM^3$  will be used in the cost volume optimization and outlier mask prediction of the fine registration.

2) *Pose Warping*: To gain an image-point cloud pair with smaller misalignment based on the coarse prior knowledge, we utilize the relative pose predicted in the coarse registration to warp the point cloud  $P^3$ . The formula is as follows:

$$(0, P_{warped}^3) = q_4(0, P^3)q_4^{-1} + (0, t_4), \quad (21)$$

where  $P_{warped}^3$  are the warped 3D coordinates of  $P^3$ .  $P_{warped}^3$ ,  $F^3$ ,  $O^3$ , and  $G^3$  are fed into the 2D-3D cost volume module using KNN-based point-pixel mixture to gain the fine 2D-3D cost volumes  $E^3$ .

3) *Optimization Module*: The fine 2D-3D cost volumes  $E^3$  are optimized with upsampled 2D-3D cost volumes  $UE^3$  to gain the optimized 2D-3D cost volumes  $OE^3 = \{oe_i^3 | i = 1, 2, \dots, N^3\}$ . The optimization enables the fine registration to utilize coarse prior knowledge. Concretely,  $E^3$ ,  $UE^3$ , and the point features of the third layer  $F^3$  are fed into a shared MLP block to gain  $OE^3$ . The formula is:

$$oe_i^3 = MLP(e_i^3 \oplus ue_i^3 \oplus f_i^3). \quad (22)$$

Then, the outlier masks of the fine registration  $M^3 = \{m_i^3 | i = 1, 2, \dots, N^3\}$  are predicted by the outlier mask prediction module. In addition, the upsampled coarse outlier masks  $UM^3$  are utilized to optimize the outlier mask prediction by coarse prior knowledge of outlier estimation. Specifically,  $OE^3$ ,  $UM^3$ , and the point features of the third layer  $F^3$  are fed into a shared MLP block to obtain  $M^3$ , as follows:

$$m_i^3 = MLP(oe_i^3 \oplus um_i^3 \oplus f_i^3). \quad (23)$$

4) *Pose Refinement*: The pose regression proposed in Section III-D3 is adopted to regress the residual relative pose  $\Delta q_3$  and  $\Delta t_3$  in the fine registration. The formula is:

$$\Delta q_3 = \frac{FC(\sum_{i=1}^{N^3} (oe_i^3 \odot mw_i^3))}{|FC(\sum_{i=1}^{N^3} (oe_i^3 \odot mw_i^3))|}, \quad (24)$$

$$\Delta t_3 = FC(\sum_{i=1}^{N^3} (oe_i^3 \odot mw_i^3)), \quad (25)$$

where the weights  $MW^3 = \{mw_i^3\}_{i=1}^{N^3}$  are as well calculated by performing softmax on the outlier masks  $M^3$ .

The residual relative pose  $\Delta q_3$  and  $\Delta t_3$  are predicted after the pose warping on  $P^3$  with  $q_4$  and  $t_4$ . Therefore,  $\Delta q_3$  and  $\Delta t_3$  refine  $q_4$  and  $t_4$  respectively to obtain the refined relative pose  $q_3$  and  $t_3$ , as follows:

$$q_3 = \Delta q_3 q_4, \quad (26)$$

$$(0, t_3) = \Delta q_3(0, t_4)\Delta q_3^{-1} + (0, \Delta t_3). \quad (27)$$

### F. Loss Function

The training loss is calculated after the forward path by comparing the output of the network and the ground truth. Inspired by LO-Net [51], two learnable parameters  $s_q$  and  $s_t$  are adopted to the loss function to bridge the scale and unit difference between the quaternion and translation vector. The loss function of single registration is as follows:

$$\mathcal{L}(q, t, q_{gt}, t_{gt}) = \|q_{gt} - q\|_2 \cdot e^{-s_q} + s_q + \|t_{gt} - t\|_1 \cdot e^{-s_t} + s_t, \quad (28)$$

where  $q_{gt}$  is the ground truth quaternion, and  $t_{gt}$  is the ground truth translation vector.  $\|\cdot\|_1$  and  $\|\cdot\|_2$  represent the  $L1$ -norm and  $L2$ -norm respectively.

Since both the coarse and refined relative poses are predicted, the total registration loss is composed of the single registration losses of the coarse and fine registrations, as follows:

$$\mathcal{L} = \alpha_3 \cdot \mathcal{L}(q_3, t_3, q_{gt}, t_{gt}) + \alpha_4 \cdot \mathcal{L}(q_4, t_4, q_{gt}, t_{gt}), \quad (29)$$



Table I  
NETWORK HYPERPARAMETERS OF I2PNET.

Module	Layer Type	$K$	$(S_h, S_w)$	Kernel Size	Distance	Channel Dimensions
Image Feature Extraction	Layer 1	—	(4,4)	—	—	[16,16,16,16,32]
	Layer 2	—	(4,4)	—	—	[32,32,32,32,64]
	Layer 3	—	(2,2)	—	—	[64,64,64,64,128]
Point Cloud Feature Extraction	Layer 1	32	(2 or 4,8)	(9,15)	0.75	[16,16,32]
	Layer 2	16	(2,2)	(9,15)	3.00	[32,32,64]
	Layer 3	16	(2,2)	(5,9)	6.00	[64,64,128]
	Layer 4	16	(1,2)	(5,9)	12.0	[128,128,256]
	Context Gathering for $E^4$	16	(1,2)	(5,9)	12.0	[128,64,64]
2D-3D Cost Volume	Layer 4 for $E^4$	$M^3$ or 32, 4	—	(3,5)	4.50	[128,64,64], [128,64], [64]
	Layer 3 for $E^3$	32, 4	—	(3,5)	4.50	[128,64,64], [128,64], [64]
Upsampling Layer	Upsampling Layer for $UE^3$	8	(1,1/2)	(5,9)	9.00	[128,64],[64]
	Upsampling Layer for $UM^3$	8	(1,1/2)	(5,9)	9.00	[128,64],[64]
Cost Volume Optimization and Outlier Mask Prediction	Cost Volume Optimization for $OE^3$	—	—	—	—	[128,64]
	Outlier Mask Prediction for $M^4$	—	—	—	—	[128,64]
	Outlier Mask Prediction for $M^3$	—	—	—	—	[128,64]
Pose Regression	FC for Middle Feature	—	—	—	—	[256]
	FC for $q^4$ , FC for $t^4$	—	—	—	—	[4], [3]
	FC for $q^3$ , FC for $t^3$	—	—	—	—	[4], [3]

where  $\mathcal{L}$  is the total registration loss of the network, and  $\alpha_3$  and  $\alpha_4$  are the weights of the single registration losses of the coarse registration and fine registration respectively.

#### IV. EXPERIMENTS

In this section, we conduct the experiments to answer the four questions and evaluate the effectiveness and efficiency of our end-to-end 2D-3D registration architecture I2PNet:

- Can end-to-end 2D-3D registration architecture localize the robot within a large range?
- Can end-to-end 2D-3D registration architecture outperform the end-to-end 2D-2D registration architectures?
- How does each module in I2PNet contribute to the end-to-end 2D-3D registration for robot localization?
- Can end-to-end 2D-3D registration architecture perform real-time image-based robot localization?

##### A. Implementation Details

We conduct all the experiments on an NVIDIA GeForce RTX 3090. PyTorch [52] is adopted to develop I2PNet. The batch sizes for both training and testing are set as 8. The Adam [53] optimizer with  $\beta_1 = 0.9$  and  $\beta_2 = 0.999$  is adopted in the training. In addition, the initial learning rate of the optimizer is set as  $10^{-3}$ , and the learning rate delays by 1% after each epoch. The weights in the total loss function are  $\alpha_3 = 0.8$ ,  $\alpha_4 = 1.6$ . The learnable parameters  $s_q$  and  $s_t$  are initialized as  $-2.5$  and  $0$  respectively. Moreover, the dropout rate for the pose regression is set as  $0.5$ .

The necessary hyperparameters of the modules in I2PNet are listed in Table I.  $(S_h, S_w)$  are the strides of the stride-based sampling in the point cloud feature extraction. In the image feature extraction,  $(S_h, S_w)$  are the strides of convolutional layers. Notably, since the initial verticle upper bounds  $H$  are set as different values for different LiDARs, the stride  $S_h$  of the first point cloud feature extraction layer is set as 2 or 4 when  $H$  is set as 32 or 64.  $K$  is the number of nearest

neighbors. Notably, the first  $K$  of 2D-3D cost volumes in the coarse registration is set as the number of pixels in the third layer  $M^3$  or 32, which represents the all-to-all point-pixel mixture or KNN-based point-pixel mixture respectively. Kernel size is the size of the 2D fixed-size kernels in the projection-aware grouping, while distance is the distance threshold in the projection-aware grouping. In image feature extraction, channel dimensions are the output channel dimensions of the convolutional layers. In the other modules, channel dimensions are the output channel dimensions of the shared MLP blocks or FC layers.

##### B. Large-Range Localization

1) *Dataset and Data Pre-processing*: The experiments are performed on the KITTI Odometry dataset [29] and nuScenes dataset [30]. In the KITTI Odometry dataset, the training set contains 0-8 sequences, and the test set includes 9-10 sequences. In the nuScenes dataset, we refer to the official split to use the 850 traversals to train our model, and 150 traversals are left for testing. The following data preprocessing are performed for the large-range localization task:

- **KITTI Odometry dataset.** We select the image-point cloud pairs from the same frame. In this setting, the image and point cloud are captured simultaneously by the RGB camera and the LiDAR that have a fixed relative position. For the LiDAR point cloud map generation, a random transformation is generated as the pose of the camera in the map coordinate system. The point cloud is transformed by the generated transformation to the map coordinate system. To localize robots with various orientations and a large range of displacement, the random transformation contains a rotation around the up-axis within  $[-2\pi, 2\pi]$  and a 2D translation on the ground within the range of  $10\text{ m}$ . The network is expected to predict the relative pose between the LiDAR point cloud map and the image to localize the robot. In addition, the

Table II  
LARGE-RANGE LOCALIZATION ERROR ON THE KITTI ODOMETRY AND nuSCENES DATASETS.

Method	KITTI Odometry		nuScenes	
	RRE ( $^{\circ}$ ) $\downarrow$	RTE (m) $\downarrow$	RRE ( $^{\circ}$ ) $\downarrow$	RTE (m) $\downarrow$
Grid. Cls. + EPnP [19]	$6.48 \pm 1.66$	$1.07 \pm 0.61$	$7.20 \pm 1.65$	$2.35 \pm 1.12$
DeepI2P (3D) [19]	$6.26 \pm 2.29$	$1.27 \pm 0.80$	$7.18 \pm 1.92$	$2.00 \pm 1.08$
DeepI2P (2D) [19]	$4.27 \pm 2.29$	$1.46 \pm 0.96$	$3.54 \pm 2.51$	$2.19 \pm 1.16$
CorrI2P [18]	$2.07 \pm 1.64$	$0.74 \pm 0.65$	$2.65 \pm 1.93$	$1.83 \pm 1.06$
Ours (I2PNet)	<b><math>0.83 \pm 1.04</math></b>	<b><math>0.21 \pm 0.29</math></b>	<b><math>1.13 \pm 1.08</math></b>	<b><math>0.75 \pm 0.59</math></b>

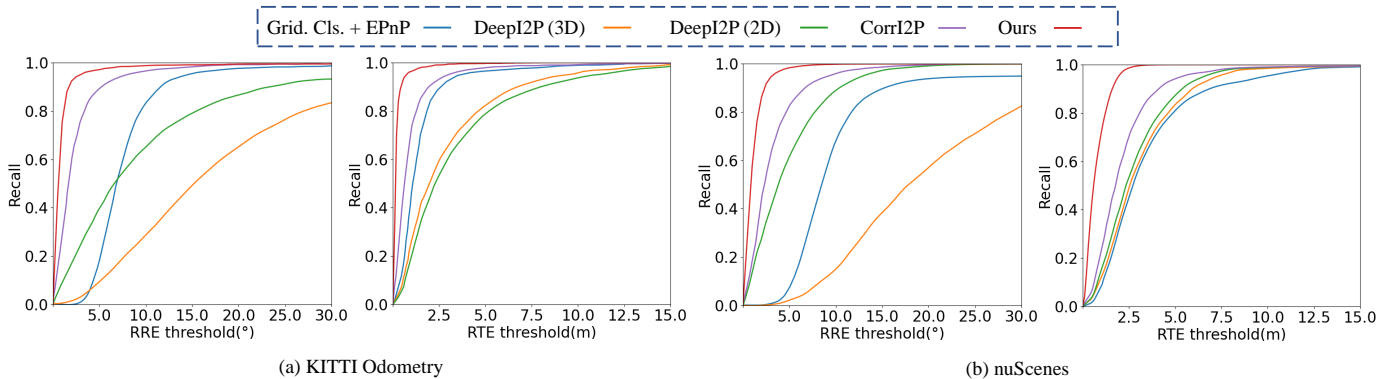


Figure 8. The registration recall curves of the methods with different RTE and RRE thresholds on KITTI Odometry and nuScenes datasets. The y-axis (recall) of the recall curve presents the success rate that RREs or RTEs are less than the threshold in the x-axis.

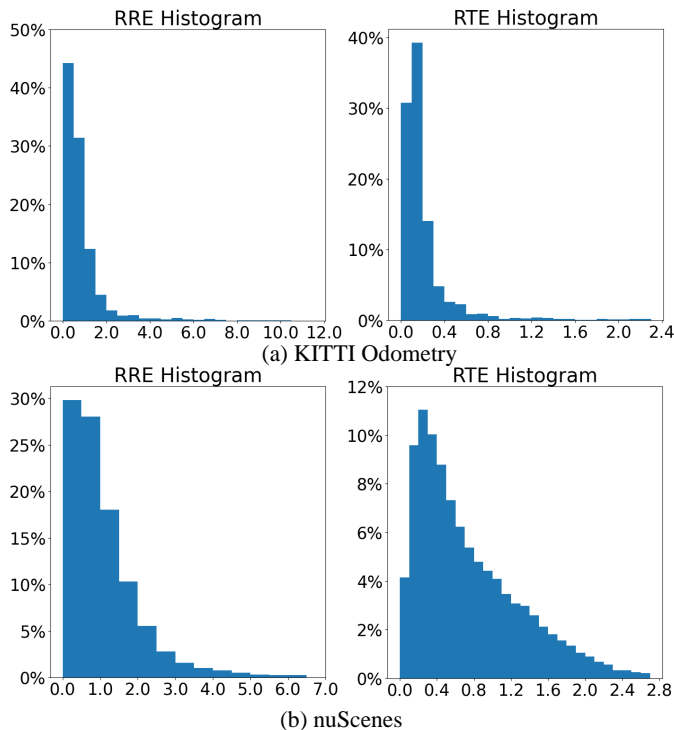


Figure 9. The histograms of RTE and RRE on the KITTI Odometry and nuScenes datasets. The x-axis is the RTE (m) or RRE ( $^{\circ}$ ), and the y-axis is the percentage falling into the corresponding bin. The bin size of RRE and RTE is  $0.5^{\circ}$  and  $0.1m$  respectively.

top 50 rows of each image are cropped because they are occupied by the sky without corresponding LiDAR points. After the cropping, the image is resized to  $160 \times 512$ . As for the point cloud, we input all the points in the LiDAR point cloud map. For the calculation of the 2D

spherical coordinates, the initial upper bounds ( $H, W$ ) are (64, 1800). The up and down vertical field-of-views are  $f_{up} = 2.0, f_{down} = 24.8$ . Moreover, for a fair comparison with other methods, each feature vector of the initial point features  $F^0$  is the concatenation of the estimated surface normal vector and the intensity.

- **nuScenes dataset.** The image and point cloud in the nearby frame are selected to form the image-point cloud pair. The known relative pose between the point cloud and the image is used to transform the point cloud. Thus, the aligned image-point cloud pair is obtained. We use the same method to form the LiDAR point cloud map as the KITTI Odometry dataset. The ranges of the rotation and translation are as well the same. In addition, the top 100 rows of each image are cropped. After the cropping, the image is resized to  $160 \times 640$ . As for the point cloud, all the points in the LiDAR point cloud map are inputted. For the calculation of the 2D spherical coordinates, the initial upper bounds ( $H, W$ ) are (32, 1800). Up and down vertical field-of-views are  $f_{up} = 10.0, f_{down} = 30.0$ . Moreover, for a fair comparison with the other methods, each feature vector of the initial point features  $F^0$  is the concatenation of a three-dimensional zero vector and the intensity.

2) *Experiment Result and Visualization:* We use the Relative Rotation Error (RRE) and the Relative Translational Error (RTE) to evaluate the performance of the models, which are calculated as:

$$RRE = \sum_{i=1}^3 |\theta_i|, \quad (30)$$

$$RTE = \|t_{pred} - t_{gt}\|_2, \quad (31)$$

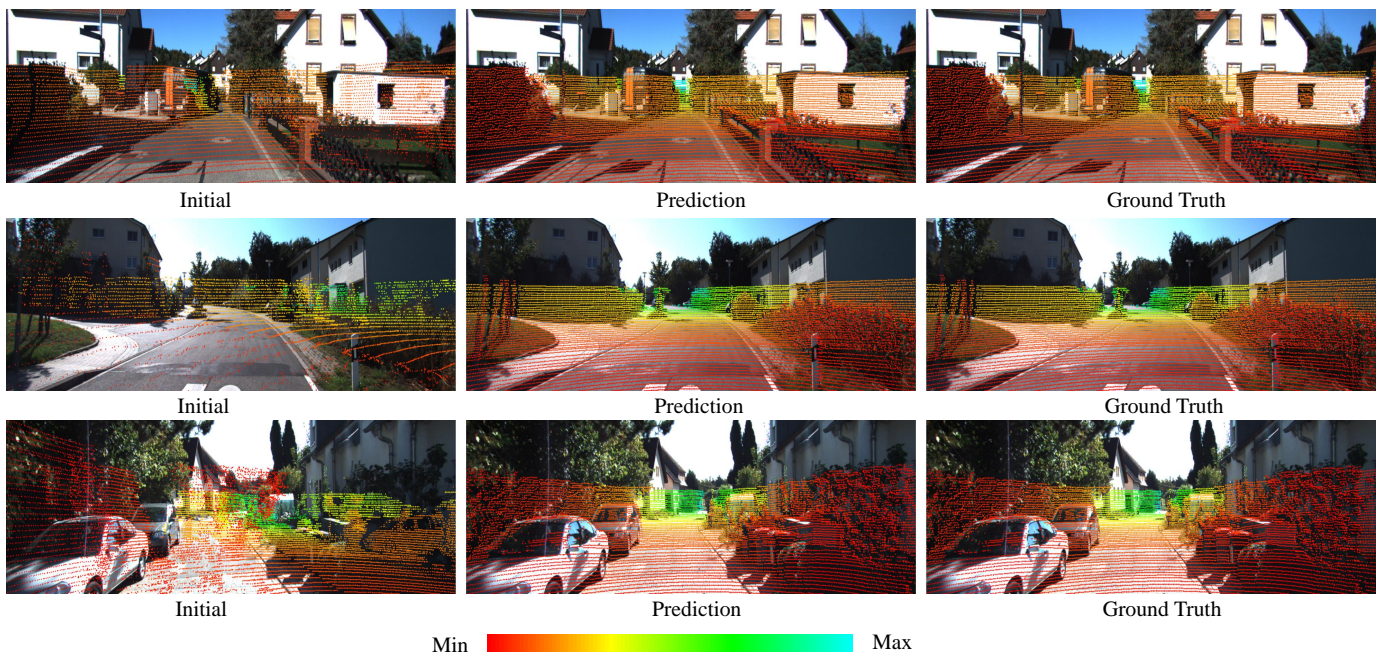


Figure 10. Visualization of large-range localization results on KITTI Odometry dataset. This figure presents the large-range localization results on KITTI Odometry dataset through the image-to-point cloud registration results. The color bar shows the depth of each LiDAR point.

where  $\{\theta_i\}_{i=1}^3$  are the Euler angles of the rotation error matrix  $R_{pred}^{-1}R_{gt}$ , where predicted rotation matrix  $R_{pred}$  is calculated by the predicted quaternion.  $R_{gt}$  is the ground truth rotation matrix of the robot pose.  $t_{pred}$  is the predicted translation vector.  $t_{gt}$  is the ground truth translation vector of the robot pose. As CorrI2P [18], we calculate the average RRE and RTE of the samples whose RREs are less than  $10^\circ$  and whose RTEs are less than  $5m$ , and the quantitative results are presented in Table II.

In Table II, we compare the performance of I2PNet with CorrI2P [18] and the three methods proposed in DeepI2P [19]. In the three methods in DeepI2P, *Grid. Cls. + EPnP* divides the image to  $32 \times 32$  patches. Then, the points falling into which patch are predicted. The predictions are used to construct the point-to-pixel correspondences. Finally, the RANSAC-based EPnP is adopted to predict the relative pose. In addition, *DeepI2P (3D)* and *DeepI2P (2D)* are the methods that predict the points falling into the image frustum, and obtain the optimal relative pose by solving the inverse camera projection problem. Their difference is that *DeepI2P (3D)* sets the relative pose of six degrees with freedom (6-DoF) in the optimization solver while *DeepI2P (2D)* sets the up-axis rotation and translation on the ground as the relative pose in the optimization solver. The results show that I2PNet outperforms the CorrI2P and three methods of DeepI2P on both two datasets. This validates that our end-to-end 2D-3D registration architecture can effectively optimize the whole registration process and more effectively localize the robot in a large range than the methods with separate modules.

The recall curves on the RRE and RTE on the KITTI Odometry dataset and nuScenes dataset are presented in Fig. 8. The results show that I2PNet has much better recall curves than the other works on both two datasets. This further shows

the localization performance of I2PNet is better than the other works. In addition, we present the RRE and RTE histograms of the predictions of I2PNet on the two datasets in Fig. 9. The histograms show that the RREs and RTEs of the predictions are mostly within the smallest error range on both two datasets.

Fig. 10 and Fig. 11 qualitatively show I2PNet’s performance on KITTI Odometry and nuScenes datasets respectively on the large-range robot localization task. For large-range robot localization, the initial misalignments between the image and point cloud are terrible as in the visualization. Despite the difficult image-point cloud pairs input, the predictions are close to the ground truths, which indicates the high localization precision of I2PNet. In addition, we also qualitatively show the effectiveness of the coarse-to-fine architecture in Fig. 12. The visualization results show that the coarse registration already generates the image-point cloud pair with a small misalignment and presents an acceptable localization precision. Moreover, the fine registration further refines the registration. Thus, the final localization error is smaller.

### C. Localization Based on Coarse Pose Initialization

The methods adopting end-to-end 2D-2D registration architectures [26]–[28] utilize the LiDAR depth image as the network input. This limits the localization range of these methods. Therefore, they require coarse pose initialization. To compare I2PNet with these methods, the localization task based on coarse pose initialization is conducted in this subsection.

1) *Dataset and Data Pre-processing*: The experiments are conducted on the KITTI Odometry dataset [29]. As the previous methods [26]–[28], the 03, 05, 06, 07, 08, and 09 sequences of the dataset are selected as the training set, and the separate 00 sequence of the dataset is selected as the test set. The global

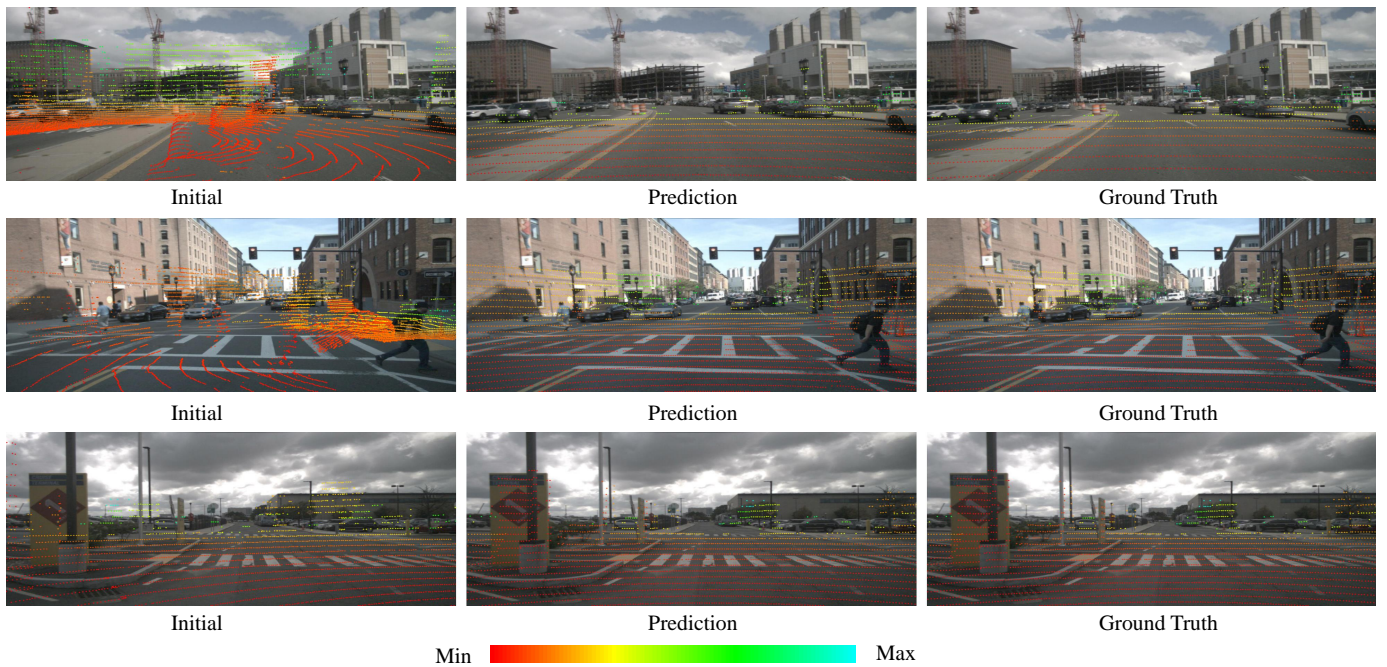


Figure 11. Visualization of large-range localization results on nuScenes dataset. This figure presents the large-range localization results on nuScenes dataset through the image-to-point cloud registration results. The color bar has the same meaning as Fig. 10.

LiDAR map is built by the frame poses provided by a LiDAR-based SLAM system. After gaining the global LiDAR point cloud map, we localize the robot with coarse pose initialization  $H_{init}$ . In addition, we crop the local 3D LiDAR map around  $H_{init}$  to limit the scale of the point cloud inputted into the network for efficient and precise feature extraction of the point cloud. Then, the local 3D LiDAR map is transformed by the coarse pose initialization  $H_{init}$  to the local map coordinate system. Thus, the localization task is to estimate the relative pose  $\phi_e$  between the local map coordinate system and the robot coordinate system, in which  $\phi_e$  is the residual pose between the coarse pose initialization and the ground truth robot pose. We simulate  $\phi_e$  by random transformation generation. Specifically,  $\phi_e$  is a composition of the random rotation within  $[-10^\circ, 10^\circ]$  and random translation within  $[-2m, 2m]$  at each of the  $x$ ,  $y$ , and  $z$  axes, which is much smaller than the range in the large-range localization task. As for the image, the top 50 rows of each image are cropped. Then, we resize the cropped image into the size  $384 \times 1280$  as the input image of the network.

As for the point cloud, we randomly sample 8192 points from the local LiDAR map as the input point cloud of the network. Notably, to fairly compare I2PNet with the 2D-2D registration architectures, the point cloud accumulation is performed to build the global LiDAR map. However, the spherical projection can only be performed on the point cloud obtained from a single scan of the rotating LiDAR. Thus, the spherical projection is not used in the experiment of this section. The vanilla neighborhood query and sampling of PointNet++ are adopted to extract the point features. Moreover, we set the initial point features  $F^0$  as the feature matrix with the size of  $8192 \times 4$ . In the feature matrix, each feature vector is the concatenation of a three-dimensional zero vector and the intensity.

2) *Experiment Result and Visualization*: We utilize the Rotation angle (Rot.) and Translation length (Transl.) of the error between the final monocular camera pose estimation and the ground truth pose to evaluate the accuracy of the localization. Specifically, since the ground truth pose is  $H_{gt} = \phi_e H_{init}$  and the final pose estimation is  $H_{final} = \phi_{pred} H_{init}$ , the error  $H_e$  between  $H_{gt}$  and  $H_{final}$  is  $H_{final} H_{gt}^{-1} = \phi_{pred} \phi_e^{-1}$ . Thus, the formulas of the Rot. and Transl. are:

$$Rot. = \arccos \frac{\text{tr}(R_e) - 1}{2}, \quad (32)$$

$$Transl. = \|t_e\|_2, \quad (33)$$

in which  $R_e$  and  $t_e$  are the rotation matrix and translation vector of  $H_e$  respectively. To validate the generalization of our model, we calculate the average median, mean, and standard deviation of the Rot. and Transl. results of ten experiments on the test set. All the results are listed in Table III. In Table III, the performance of I2PNet is compared with the end-to-end 2D-2D registration-based methods [26]–[28]. In addition, for complete comparison, the conventional method CASELITZ [14] and the RANSAC-based method CMRNet++ [21], are as well included in the comparison. The results in Table III indicate that our I2PNet has the smallest final pose estimation error. Compared to CASELITZ, I2PNet only requires a single image rather than the local bundle adjustment reconstruction from image sequences since the 2D-3D cost volume module can directly match the pixels and points. Compared to CMRNet++, I2PNet is an end-to-end architecture, while CMRNet++ adopts the separate RANSAC-based pose estimation module. As in the large-range localization task, I2PNet benefits from end-to-end optimization and thus has better localization accuracy. Compared to the end-to-end 2D-2D registration-based methods [26]–[28], I2PNet does not use the 2D correlation between the depth map and

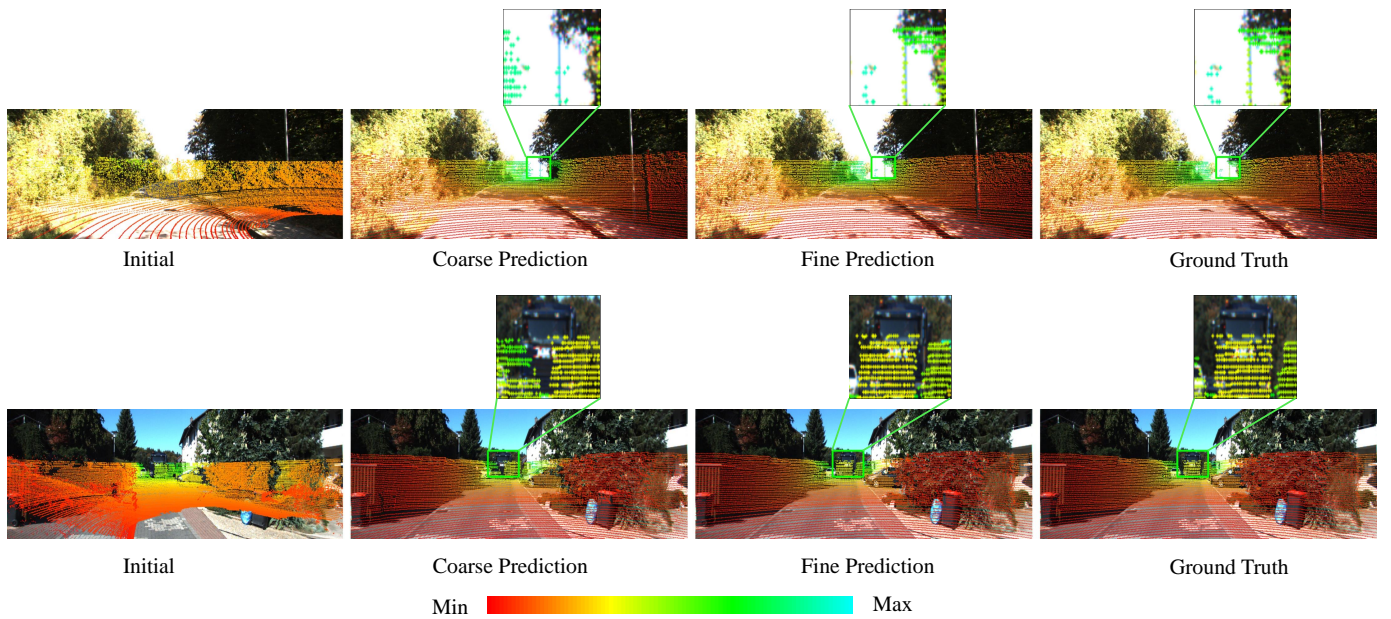


Figure 12. Visualization of coarse and fine registration results. The coarse and fine predictions are obtained in the coarse and fine registration respectively. The zoom-in views of the areas marked by the bounding boxes in each picture are to better present the difference among the coarse prediction, fine prediction, and ground truth. The color bar has the same meaning as Fig. 10.

the image but utilizes the 2D-3D cost volume module to directly estimate the correspondences between the raw 3D point cloud and image. The depth map is an indirect representation of the point cloud and depends on the camera intrinsic. Therefore, I2PNet using the 2D-3D registration performs better localization.

Fig. 13 qualitatively shows the camera localization performance of I2PNet. The prediction results show that the projected LiDAR maps are well-aligned with the images after being transformed by the predicted camera poses. The results further indicate that I2PNet can effectively localize the robot equipped with a monocular camera in the LiDAR point cloud map with coarse pose initialization.

#### D. Ablation Studies

In this subsection, we conduct ablation studies to discuss the effect of the input point number and the effectiveness of the proposed modules. Our ablation studies are all conducted on the large-range localization task with the KITTI Odometry dataset.

1) *Effect of the Input Point Number*: In Section III-B, we introduce the stride-based sampling and projection-aware grouping to replace FPS and neighborhood query among all the points in vanilla PointNet++. The replacement makes us able to process all the points in the raw point cloud efficiently. The network using all the points can fully utilize the information of the raw point cloud and thus has a better localization performance. To validate this, we compare the RRE/RTE localization error between the network using fixed-size points and the network using all the points. We also set different numbers of the input points as 8192, 16384, and 24576. The results in Table IV show that the increment of input points number can effectively improve the localization

performance. Moreover, the network using all the points has the best performance. In Section IV-E, we will show the network using all the points is still efficient.

2) *Effectiveness of the Proposed Modules*: We also conduct ablation studies to show the effectiveness of the proposed modules. In the subsequent ablation studies, despite the mentioned differences, the modules and hyperparameters are the same as the proposed I2PNet.

- **Effectiveness of the proposed 2D-3D cost volume module.** In the ablation study, *Ours (w/o 2D-3D Cost Volume Module)*, the image-to-point cloud attentive fusion module proposed by DeepI2P [19] is used to replace the 2D-3D cost volume module. The attentive fusion module of DeepI2P performs the attentive aggregation of the image features for each point. Then, the aggregated point-wise image features are fused with the point features by concatenation. The quantitative results of *Ours (w/o 2D-3D Cost Volume Module)* in Table V show that the localization performance decreases after replacing the 2D-3D cost volume module with a simple cross-modality fusion module. The decrement indicates that 2D-3D association is not a simple cross-modality feature fusion. Our 2D-3D cost volume module implicitly constructs the point-pixel correspondences and embeds essential position information for spatial transformation estimation. In contrast, the attentive fusion module just performs the cross-modality feature fusion. Thus, the network using the simple attentive fusion module has a larger relative rotation error and can hardly learn to register the image and point cloud in the aspect of translation.
- **Effectiveness of the outlier mask prediction module.** In the ablation study, *Ours (w/o Outlier Mask)*, the global spatial transformation embedding feature is the simple average pooling of the 2D-3D cost volumes rather than

Table III  
LOCALIZATION ERROR WITH COARSE POSE INITIALIZATION ON KITTI ODOMETRY DATASET

Method	Rot. (°) ↓	Transl. (m) ↓	Median Rot. (°) ↓	Median Transl. (m) ↓
CASELITZ [14]	1.65 ± 0.91	0.30 ± 0.11	—	—
CMRNet [26]	—	—	1.39	0.51
CMRNet++ [21]	—	—	1.46	0.55
HyperMap [27]	—	—	1.42	0.48
I2D-Loc [28]	—	—	0.70	0.18
Ours (I2PNet)	<b>0.74 ± 0.40</b>	<b>0.08 ± 0.06</b>	<b>0.67</b>	<b>0.07</b>

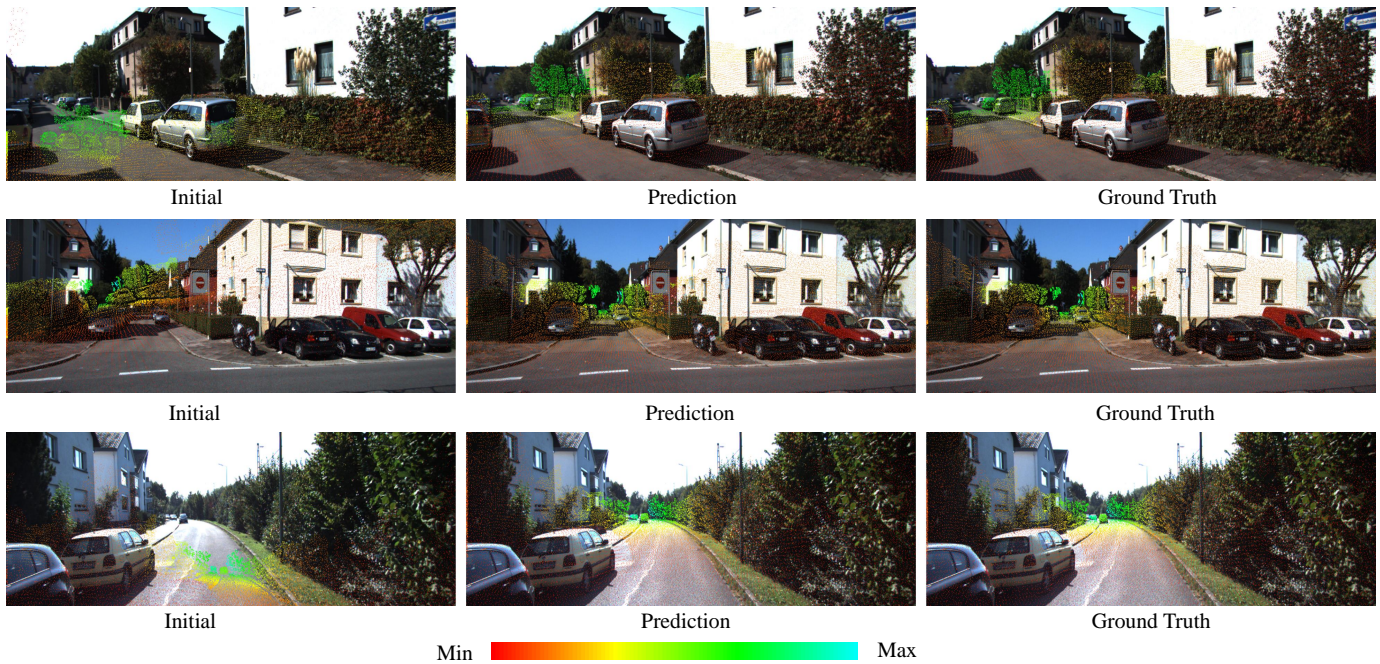


Figure 13. Visualization of localization with coarse pose initialization. The visualization results present the localization quality on 00 sequence of the KITTI Odometry dataset. Notably, the presented results are processed by the occlusion filtering method proposed in CMRNet [26] for better visualization. The color bar has the same meaning as Fig. 10.

Table IV  
ABLATION STUDY ON THE NUMBER OF INPUT POINTS

Method	RRE (°) ↓	RTE (m) ↓
Ours (w/ 8192 input points)	2.16 ± 1.90	0.57 ± 0.37
Ours (w/ 16384 input points)	2.05 ± 1.85	0.48 ± 0.36
Ours (w/ 24576 input points)	1.61 ± 1.42	0.36 ± 0.29
Ours (w/ all input points)	<b>0.83 ± 1.04</b>	<b>0.21 ± 0.29</b>

Table VI  
EFFICIENCY ANALYSIS.

Method	Network size (MB)	Inference (s)
Grid. Cls. + EPnP [19]	100.75	0.051
DeepI2P (3D) [19]	100.12	16.588
DeepI2P (2D) [19]	100.12	9.388
CorrI2P [18]	141.07	2.984
Ours (I2PNet) (8192 w/o projection)	<b>3.38</b>	0.069
Ours (I2PNet) (16384 w/o projection)	<b>3.38</b>	0.143
Ours (I2PNet) (24576 w/o projection)	<b>3.38</b>	0.271
Ours (I2PNet) (all points w/ projection)	<b>3.38</b>	<b>0.048</b>

Table V  
ABLATION STUDY ON THE EFFECTIVENESS OF THE PROPOSED MODULES

Method	RRE (°) ↓	RTE (m) ↓
Ours (w/o 2D-3D Cost Volume Module)	2.54 ± 1.94	3.29 ± 1.19
Ours (w/o Outlier Mask)	1.12 ± 1.28	0.28 ± 0.27
Ours (w/o Fine Registration)	1.59 ± 1.41	0.60 ± 0.60
Ours (w/o Pose Warping)	1.63 ± 1.41	0.53 ± 0.54
Ours (w/o LST Embedding)	1.01 ± 1.13	0.29 ± 0.33
Ours (I2PNet)	<b>0.83 ± 1.04</b>	<b>0.21 ± 0.29</b>

the weighted sum of the 2D-3D cost volumes with the weights of the outlier masks. The quantitative results of

*Ours (w/o Outlier Mask)* in Table V show that the learned outlier masks can effectively filter the outliers and thus result in a smaller localization error.

- **Effectiveness of the fine registration.** In the ablation study, *Ours (w/o Fine Registration)*, only the coarse registration is performed. The quantitative results of *Ours (w/o Fine Registration)* in Table V show that the coarse-to-fine registration architecture results in better registration performance. More correct correspondences can be found

Table VII  
ONLINE CALIBRATION METRICS ON THE KITTI RAW DATASET.

Method	T1		T2a		T2b		T3	
	MSEE ↓	MRR ↑	MSEE ↓	MRR ↑	MSEE ↓	MRR ↑	MSEE ↓	MRR ↑
$\beta$ -RegNet [42]	0.0480	53.23%	0.0440	37.08%	0.0460	34.14%	0.0920	-1.89%
TAYLOR [54]	-	-	-	-	-	-	0.0100	-
CalibNet [44]	-	-	0.0220	-	0.0220	-	-	-
RGGNet [45]	0.0210	78.40%	0.0140	75.61%	0.0170	72.64%	0.0100	83.22%
Ours (I2PNet)	<b>0.00096</b>	<b>99.04%</b>	<b>0.00084</b>	<b>98.61%</b>	<b>0.00115</b>	<b>97.81%</b>	<b>0.00154</b>	<b>97.21%</b>

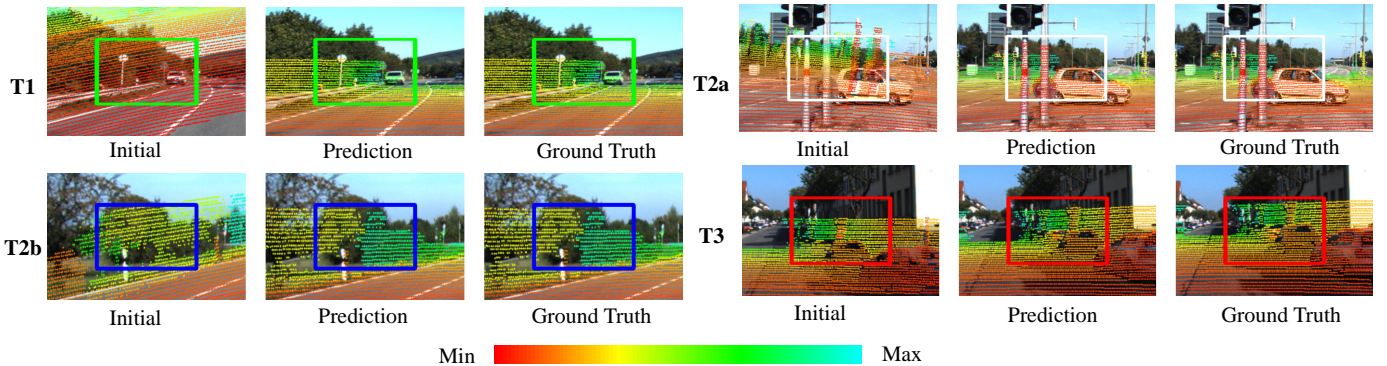


Figure 14. Visualization of online calibration results. This figure presents the online calibration results on the four test sets. The pictures are cropped for better presentation and the areas that can reflect the calibration quality are marked by the bounding boxes. The color bar has the same meaning as Fig. 10.

in the refined image-point cloud pair and thus make the predicted relative pose more accurate.

- **Effectiveness of the pose warping.** In the ablation study, *Ours (w/o Pose Wrapping)*, we do not warp the point cloud before estimating the 2D-3D cost volumes in the fine registration. The quantitative results of *Ours (w/o Pose Wrapping)* in Table V show that pose warping is essential for the coarse-to-fine architecture and can improve the registration performance because it generates an image-point cloud pair with smaller misalignment.
- **Effectiveness of the LST Embedding.** In the ablation study, *Ours (w/o LST Embedding)*, we directly output the implicit correspondence features as the 2D-3D cost volumes. The quantitative results of *Ours (w/o LST Embedding)* in Table V show that the embedded spatial transformation improves the outlier mask prediction. Therefore, the localization is more accurate.

### E. Efficiency Evaluation

In this subsection, we conduct the efficiency evaluation to validate the efficiency improvement of I2PNet to the previous works by the end-to-end 2D-3D registration architecture for the large-range robot localization. We present the evaluation results in Table VI. The results of *Grid. Cls. + EPnP*, *DeepI2P (3D)*, *DeepI2P (2D)*, *CorrI2P*, and the I2PNets with different numbers of input points as the setting in Section IV-D are presented. For the former four methods, the inference time includes the pose estimation post-processing time evaluated on Intel(R) Xeon(R) Gold 6346 CPU and network inference time evaluated on an NVIDIA GeForce RTX 3090. I2PNet does not need the pose estimation post-processing. Thus, the inference time only includes the network inference time. From

the efficiency comparison between the I2PNets with different numbers of input points in Table VI, we can conclude that the efficiency of the I2PNets with the vanilla sampling and neighborhood query methods decreases when the number of points increases. In contrast, by using efficient stride-based sampling and projection-aware grouping to replace the vanilla sampling and neighborhood query methods, the final proposed I2PNet using all input points has better efficiency than the I2PNets using fixed-size input points. Moreover, the final proposed I2PNet also has better efficiency than all the previous works. This supports our argument that our proposed end-to-end structure performs more accurate and efficient registration compared to the previous methods with the separate pose estimation module.

### V. EXTENSION TO CAMERA-LIDAR ONLINE CALIBRATION

In this section, we demonstrate the effectiveness of I2PNet when extended to the camera-LiDAR online calibration task.

1) *Dataset and Data Pre-processing:* Like the recent camera-LiDAR online calibration methods [42], [44], [45], [54], the KITTI raw dataset [29] is adopted to evaluate our network. The same training set and test set are chosen as the recent methods. Before describing the setting of the training and test sets, the method that generates the dataset is first introduced: The ground truth extrinsic calibration matrix between each camera-LiDAR pair  $H_{gt}$  is first calculated with the calibration data provided by the KITTI raw dataset. We adopt the method as RGGNet [45] to simulate the calibration error during the running of the robot. Specifically,  $H_{gt}$  is randomly varied to obtain the initial calibration matrix  $H_{initial}$  with calibration error, as follows:

$$H_{initial} = \phi H_{gt}, \quad (34)$$

where  $\phi$  is a random transformation matrix with the uniformly sampled translation error within the range of  $\pm\gamma m$  in each translation axis and uniformly sampled rotation error within the range of  $\pm\beta^\circ$  in each rotation axis. Then, we use the initial calibration matrix  $H_{initial}$  to multiply the original coordinates of the LiDAR points to obtain the LiDAR point cloud with the calibration error. Because  $H_{gt}$  is the ground truth calibration matrix,  $\phi$  is exactly the calibration error between the new point cloud and the image. Therefore, our network is to estimate the ground truth decalibration matrix  $\phi_{gt}$ , which is exactly the relative pose between the image and the new point cloud.  $\phi_{gt}$  is calculated as follows:

$$\phi_{gt} = \phi^{-1}. \quad (35)$$

$\phi_{gt}$  is transformed to the equivalent quaternion  $q_{gt}$  and translation vector  $t_{gt}$ . By the dataset generation method, we generate the training set from all the drives except the 0005 and 0070 drives in the 09/26/2011 sequence of KITTI raw dataset. For a fair comparison with the recent methods, the training set consists of the following three subsets randomly sampled from the whole data: (1) 24000 samples with the calibration error range ( $\pm 0.2m, \pm 15^\circ$ ) for the training on both the rotation and the translation errors; (2) 3000 samples with the calibration error range ( $\pm 0.3m, \pm 0^\circ$ ) for the training on the pure translation error; (3) 3000 samples with error ( $\pm 0m, \pm 20^\circ$ ) for the training on the pure rotation error. For the test set, the four different test sets are generated as well for a fair comparison: (1) **T1** consists of 2000 samples randomly sampled from the 0005 and 0070 drives in 09/26/2011 sequence with the calibration error range ( $\pm 0.2m, \pm 15^\circ$ ); (2) **T2a** consists of 2000 samples randomly sampled from all the drives except the 0005 and 0070 drives in 09/26/2011 sequence with the calibration error range ( $\pm 0.2m, \pm 10^\circ$ ); (3) **T2b** consists of 2000 samples randomly sampled from the 0005 and 0070 drives in 09/26/2011 sequence with the calibration error range ( $\pm 0.2m, \pm 10^\circ$ ); (4) **T3** consists of 2000 samples randomly sampled from the 0027 drive in 10/03/2011 sequence with the calibration error range ( $\pm 0.3m, \pm 2^\circ$ ) for the comparison with the conventional methods [54]. It is noticed that RGGNet [45] utilizes the independently sampled 2000 samples with the calibration error range ( $\pm 0.3m, \pm 2^\circ$ ) on the 0027 drive in 10/03/2011 sequence to finetune the model. In contrast, we do not finetune our model on the extra training data. In addition, we resize the input image to  $352 \times 1216$  and input all the points in the raw point cloud. For the calculation of the 2D spherical coordinates, the initial upper bounds ( $H, W$ ) are (64, 1800). Up and down vertical field-of-views are  $f_{up} = 2.0$ ,  $f_{down} = 24.8$ . Moreover, each feature vector of the initial point features  $F^0$  is the concatenation of a three-dimensional zero vector and the intensity.

2) *Experiment Result and Visualization*: Table VII presents the quantitative experiment results between the I2PNet and the other works on the four test sets.  $\beta$ -RegNet is the re-implemented RegNet [42] by RGGNet [45] which uses the network architecture of RGGNet [45] and the loss in RegNet [42]. In the experiment results, we utilize the same evaluation metrics as RGGNet [45]: mean *se3* error (MSEE) and mean re-calibration rate (MRR). MSEE and MRR are

based on the *se3* distance between the predicted decalibration matrix  $\phi_{pred}$  (which is calculated using the predicted  $q_3$  and  $t_3$ ) and ground truth decalibration matrix  $\phi_{gt}$ . The formulas of the metrics are:

$$MSEE = \frac{1}{n} \sum_{i=1}^n E_i, \quad (36)$$

$$MRR = \frac{1}{n} \sum_{i=1}^n \frac{\eta_i - E_i}{\eta_i}, \quad (37)$$

where  $E_i$  is the *se3* distance between  $\phi_{pred}$  and  $\phi_{gt}$  of the  $i$ -th sample,  $n$  is the number of samples, and  $\eta_i$  is the miscalibration noise of the  $i$ -th sample.

As shown in Table VII, our I2PNet has better MSEEs and MRRs than all the state-of-the-art works in all the test sets by a large margin. The results show that I2PNet is effectively extended to the online calibration task with high calibration accuracy. This indicates that the end-to-end 2D-3D registration architecture enables the wider application of I2PNet in various robot tasks and results in better registration. In addition, it is noticed that on the T3 test set, I2PNet has better performance than the finetuned RGGNet and the traditional method TAYLOR without finetuning. The performance on the T3 test set shows that I2PNet is robust to various initial noise ranges.

Fig. 14 qualitatively shows the online calibration performance of I2PNet. The visualization shows that the initial misalignments on T1, T2a, and T2b test sets are large, while the initial misalignment on the T3 test set is small. Despite the different initial misalignments, the predictions made by I2PNet have few differences from the ground truths on all four test sets. These results further demonstrate the effectiveness and generality of I2PNet on the camera-LiDAR online calibration task.

## VI. CONCLUSION

In this paper, we introduce a novel image-to-point cloud registration architecture, I2PNet, for vehicle localization. I2PNet performs both high accuracy and efficient large-range image-based robot localization in the LiDAR point cloud map based on the end-to-end 2D-3D registration. We realize the end-to-end 2D-3D registration by the novel 2D-3D cost volume module and outlier mask prediction module. The coarse-to-fine 2D-3D registration is further proposed for finer registration and better localization. The end-to-end 2D-3D registration enables each module to be optimized by the unique target. In addition, the complete 3D point cloud structure is preserved for the image-to-point cloud association in the architecture. Therefore, better registration accuracy is realized.

We conduct extensive experiments on multiple datasets and tasks to demonstrate the state-of-the-art camera localization ability in the LiDAR point cloud map of I2PNet. I2PNet can reach  $0.83^\circ$  average RRE and  $0.21m$  average RTE within a large localization range of  $360^\circ$  and  $10m$  on the KITTI Odometry dataset, improving 60.0% average RRE and 71.6% average RTE than the previous state-of-the-art methods. In addition, the performance of the same task on nuScenes dataset as well exceeds previous methods. Specifically, I2PNet reaches



1.13° average RRE and 0.75m average RTE, improving 57.4% average RRE and 59.0% average RTE than the state-of-the-art method. Moreover, based on the end-to-end architecture, the efficiency of I2PNet reaches real-time, which is 48ms, outperforming the previous methods. I2PNet also outperforms the previous end-to-end 2D-2D registration-based methods which require coarse pose initialization. The median rotation error and median translation error of I2PNet are 0.67° and 0.07m, improving the best 0.70° median rotation error and 0.18m median translation error of the previous methods by 4.3% and 61.1% respectively. As for the extension of I2PNet to camera-LiDAR online calibration, I2PNet reaches 98.17% average re-calibration rate, exceeding the best 77.47% average re-calibration rate of previous online calibration methods by 26.7%.

Finally, the source code will be released upon the acceptance of this paper.

## REFERENCES

- [1] P. J. Besl and N. D. McKay, "Method for registration of 3-d shapes," in *Sensor fusion IV: control paradigms and data structures*, vol. 1611, 1992, pp. 586–606.
- [2] J. Yang, H. Li, and Y. Jia, "Go-icp: Solving 3d registration efficiently and globally optimally," in *Proc. Int. Conf. Comput. Vis.*, 2013, pp. 1457–1464.
- [3] Z. Liu, S. Zhou, C. Suo, P. Yin, W. Chen, H. Wang, H. Li, and Y.-H. Liu, "Lpd-net: 3d point cloud learning for large-scale place recognition and environment analysis," in *Proc. Int. Conf. Comput. Vis.*, 2019, pp. 2831–2840.
- [4] W. Lu, G. Wan, Y. Zhou, X. Fu, P. Yuan, and S. Song, "Deepvcp: An end-to-end deep neural network for point cloud registration," in *Proc. Int. Conf. Comput. Vis.*, 2019, pp. 12–21.
- [5] Z. J. Yew and G. H. Lee, "Rpm-net: Robust point matching using learned features," in *Proc. IEEE Conf. Comput. Vis. Pattern Recognit.*, 2020, pp. 11 824–11 833.
- [6] D. Cattaneo, M. Vaghi, and A. Valada, "Lcdnet: Deep loop closure detection and point cloud registration for lidar slam," *IEEE Trans. Robot.*, 2022.
- [7] D. G. Lowe, "Object recognition from local scale-invariant features," in *Proc. Int. Conf. Comput. Vis.*, vol. 2, 1999, pp. 1150–1157.
- [8] Y. Ke and R. Sukthankar, "Pca-sift: A more distinctive representation for local image descriptors," in *Proc. IEEE Comput. Soc. Conf. Comput. Vision Pattern Recogn.*, vol. 2, 2004, pp. II–II.
- [9] T. Sattler, B. Leibe, and L. Kobbelt, "Fast image-based localization using direct 2d-to-3d matching," in *Proc. Int. Conf. Comput. Vis.*, 2011, pp. 667–674.
- [10] T. Sattler, B. Leibe, and L. Kobbelt, "Efficient & effective prioritized matching for large-scale image-based localization," *IEEE Trans. Pattern Anal. Mach. Intell.*, vol. 39, no. 9, pp. 1744–1756, 2016.
- [11] K. M. Yi, E. Trulls, V. Lepetit, and P. Fua, "Lift: Learned invariant feature transform," in *Proc. Eur. Conf. Comput. Vis.*, 2016, pp. 467–483.
- [12] R. W. Wolcott and R. M. Eustice, "Visual localization within lidar maps for automated urban driving," in *Proc. Int. Conf. Intell. Robots Syst. IEEE*, 2014, pp. 176–183.
- [13] G. Pascoe, W. Maddern, and P. Newman, "Direct visual localisation and calibration for road vehicles in changing city environments," in *Proceedings of the IEEE International Conference on Computer Vision Workshops*, 2015, pp. 9–16.
- [14] T. Caselitz, B. Steder, M. Ruhnke, and W. Burgard, "Monocular camera localization in 3d lidar maps," in *Proc. Int. Conf. Intell. Robots Syst.*, 2016, pp. 1926–1931.
- [15] H. Qiao, Y.-X. Wu, S.-L. Zhong, P.-J. Yin, and J.-H. Chen, "Brain-inspired intelligent robotics: Theoretical analysis and systematic application," *Mach. Intell. Res.*, vol. 20, no. 1, pp. 1–18, 2023.
- [16] M. Feng, S. Hu, M. H. Ang, and G. H. Lee, "2d3d-matchnet: Learning to match keypoints across 2d image and 3d point cloud," in *Proc. IEEE Int. Conf. Robot. Autom.*, 2019, pp. 4790–4796.
- [17] B. Wang, C. Chen, Z. Cui, J. Qin, C. X. Lu, Z. Yu, P. Zhao, Z. Dong, F. Zhu, N. Trigoni *et al.*, "P2-net: Joint description and detection of local features for pixel and point matching," in *Proc. Int. Conf. Comput. Vis.*, 2021, pp. 16004–16013.
- [18] S. Ren, Y. Zeng, J. Hou, and X. Chen, "Corri2p: Deep image-to-point cloud registration via dense correspondence," *IEEE Trans. Circuits Syst. Video Technol.*, 2022.
- [19] J. Li and G. H. Lee, "Deepi2p: Image-to-point cloud registration via deep classification," in *Proc. IEEE Conf. Comput. Vis. Pattern Recognit.*, 2021, pp. 15 960–15 969.
- [20] Y. Jeon and S.-W. Seo, "Efgnet: A versatile image-to-point cloud registration network for extreme outdoor environment," *IEEE Robot. Autom. Lett.*, vol. 7, no. 3, pp. 7511–7517, 2022.
- [21] D. Cattaneo, D. G. Sorrenti, and A. Valada, "Cmrnet++: Map and camera agnostic monocular visual localization in lidar maps," *arXiv:2004.13795*, 2020.
- [22] M. A. Fischler and R. C. Bolles, "Random sample consensus: a paradigm for model fitting with applications to image analysis and automated cartography," *Commun. ACM*, vol. 24, no. 6, pp. 381–395, 1981.
- [23] Y. I. Abdel-Aziz, H. M. Karara, and M. Hauck, "Direct linear transformation from comparator coordinates into object space coordinates in close-range photogrammetry," *Photogramm. Eng. Remote Sens.*, vol. 81, no. 2, pp. 103–107, 2015.
- [24] V. Lepetit, F. Moreno-Noguer, and P. Fua, "Epnnp: An accurate o (n) solution to the pnp problem," *Int. J. Comput. Vis.*, vol. 81, no. 2, pp. 155–166, 2009.
- [25] D. W. Marquardt, "An algorithm for least-squares estimation of nonlinear parameters," *J. Soc. Ind. Appl. Math.*, vol. 11, no. 2, pp. 431–441, 1963.
- [26] D. Cattaneo, M. Vaghi, A. L. Ballardini, S. Fontana, D. G. Sorrenti, and W. Burgard, "Cmrnet: Camera to lidar-map registration," in *Proc. IEEE Intell. Transp. Syst. Conf.*, 2019, pp. 1283–1289.
- [27] M.-F. Chang, J. Mangelson, M. Kaess, and S. Lucey, "Hypermap: Compressed 3d map for monocular camera registration," in *2021 IEEE International Conference on Robotics and Automation (ICRA)*. IEEE, 2021, pp. 11 739–11 745.
- [28] K. Chen, H. Yu, W. Yang, L. Yu, S. Scherer, and G.-S. Xia, "I2d-loc: Camera localization via image to lidar depth flow," *ISPRS Journal of Photogrammetry and Remote Sensing*, vol. 194, pp. 209–221, 2022.
- [29] A. Geiger, P. Lenz, C. Stiller, and R. Urtasun, "Vision meets robotics: The kitti dataset," *Int. J. Robot. Res.*, vol. 32, no. 11, pp. 1231–1237, 2013.
- [30] H. Caesar, V. Bankiti, A. H. Lang, S. Vora, V. E. Liong, Q. Xu, A. Krishnan, Y. Pan, G. Baldan, and O. Beijbom, "nusenes: A multimodal dataset for autonomous driving," in *Proc. IEEE Conf. Comput. Vis. Pattern Recognit.*, 2020, pp. 11 621–11 631.
- [31] Y. Zhong, "Intrinsic shape signatures: A shape descriptor for 3d object recognition," in *Proc. Int. Conf. Comput. Vis Workshops*, 2009, pp. 689–696.
- [32] M. J. Black and P. Anandan, "The robust estimation of multiple motions: Parametric and piecewise-smooth flow fields," *Comput. Vis. Image Underst.*, vol. 63, no. 1, pp. 75–104, 1996.
- [33] T. Brox, A. Bruhn, N. Papenbergh, and J. Weickert, "High accuracy optical flow estimation based on a theory for warping," in *Proc. Eur. Conf. Comput. Vis.*, 2004, pp. 25–36.
- [34] D. Sun, X. Yang, M.-Y. Liu, and J. Kautz, "Pwc-net: Cnns for optical flow using pyramid, warping, and cost volume," in *Proc. IEEE Conf. Comput. Vis. Pattern Recognit.*, 2018, pp. 8934–8943.
- [35] W. Wu, Z. Y. Wang, Z. Li, W. Liu, and L. Fuxin, "Pointpwc-net: Cost volume on point clouds for (self-) supervised scene flow estimation," in *Proc. Eur. Conf. Comput. Vis.*, 2020, pp. 88–107.
- [36] G. Wang, X. Wu, Z. Liu, and H. Wang, "Hierarchical attention learning of scene flow in 3d point clouds," *IEEE Transactions on Image Processing*, vol. 30, pp. 5168–5181, 2021.
- [37] G. Wang, Y. Hu, Z. Liu, Y. Zhou, M. Tomizuka, W. Zhan, and H. Wang, "What matters for 3d scene flow network," in *Proc. Eur. Conf. Comput. Vis.*, 2022, pp. 38–55.
- [38] G. Wang, X. Wu, Z. Liu, and H. Wang, "Pwclw-net: Deep lidar odometry in 3d point clouds using hierarchical embedding mask optimization," in *Proc. IEEE Conf. Comput. Vis. Pattern Recognit.*, 2021, pp. 15 910–15 919.
- [39] S. Bileschi, "Fully automatic calibration of lidar and video streams from a vehicle," in *Proc. Int. Conf. Comput. Vis. Workshops*. IEEE, 2009, pp. 1457–1464.
- [40] J. Levinson and S. Thrun, "Automatic online calibration of cameras and lasers," in *Proc. Robot.: Sci. Syst. Conf*, vol. 2, 2013, p. 7.
- [41] G. Pandey, J. R. McBride, S. Savarese, and R. M. Eustice, "Automatic extrinsic calibration of vision and lidar by maximizing mutual information," *J. Field Robot.*, vol. 32, no. 5, pp. 696–722, 2015.
- [42] N. Schneider, F. Piewak, C. Stiller, and U. Franke, "Regnet: Multimodal sensor registration using deep neural networks," in *IEEE Intell. Veh. Symp. Proc.*, 2017, pp. 1803–1810.

- [43] M. Lin, Q. Chen, and S. Yan, "Network in network," *arXiv:1312.4400*, 2013.
- [44] G. Iyer, R. K. Ram, J. K. Murthy, and K. M. Krishna, "Calibnet: Geometrically supervised extrinsic calibration using 3d spatial transformer networks," in *Proc. Int. Conf. Intell. Robots Syst.*, 2018, pp. 1110–1117.
- [45] K. Yuan, Z. Guo, and Z. J. Wang, "Rgnet: Tolerance aware lidar-camera online calibration with geometric deep learning and generative model," *IEEE Robot. Autom. Lett.*, vol. 5, no. 4, pp. 6956–6963, 2020.
- [46] C. R. Qi, L. Yi, H. Su, and L. J. Guibas, "Pointnet++: Deep hierarchical feature learning on point sets in a metric space," in *Proc. Adv. Neural Inf. Process. Syst.*, 2017, pp. 5099–5108.
- [47] C. R. Qi, H. Su, K. Mo, and L. J. Guibas, "Pointnet: Deep learning on point sets for 3d classification and segmentation," in *Proc. IEEE Conf. Comput. Vis. Pattern Recognit.*, 2017, pp. 652–660.
- [48] G. Wang, X. Wu, S. Jiang, Z. Liu, and H. Wang, "Efficient 3d deep lidar odometry," *IEEE Trans. Pattern Anal. Mach. Intell.*, 2022.
- [49] B. Wu, A. Wan, X. Yue, and K. Keutzer, "Squeezeseg: Convolutional neural nets with recurrent crf for real-time road-object segmentation from 3d lidar point cloud," in *Proc. IEEE Int. Conf. Robot. Autom.*, 2018, pp. 1887–1893.
- [50] Q. Hu, B. Yang, L. Xie, S. Rosa, Y. Guo, Z. Wang, N. Trigoni, and A. Markham, "Randla-net: Efficient semantic segmentation of large-scale point clouds," in *Proc. IEEE Conf. Comput. Vis. Pattern Recognit.*, 2020, pp. 11 108–11 117.
- [51] Q. Li, S. Chen, C. Wang, X. Li, C. Wen, M. Cheng, and J. Li, "Lo-net: Deep real-time lidar odometry," in *Proc. IEEE Conf. Comput. Vis. Pattern Recognit.*, 2019, pp. 8473–8482.
- [52] A. Paszke, S. Gross, F. Massa, A. Lerer, J. Bradbury, G. Chanan, T. Killeen, Z. Lin, N. Gimelshein, L. Antiga *et al.*, "Pytorch: An imperative style, high-performance deep learning library," *Proc. Adv. Neural Inf. Process. Syst.*, vol. 32, pp. 8026–8037, 2019.
- [53] D. P. Kingma and J. Ba, "Adam: A method for stochastic optimization," *arXiv:1412.6980*, 2014.
- [54] Z. Taylor and J. Nieto, "Motion-based calibration of multimodal sensor extrinsics and timing offset estimation," *IEEE Trans. Robot.*, vol. 32, no. 5, pp. 1215–1229, 2016.



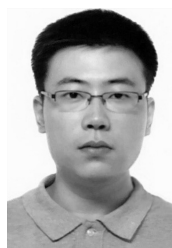
**Guangming Wang** received the B.S. degree from Department of Automation from Central South University, Changsha, China, in 2018. He is currently pursuing the Ph.D. degree in Control Science and Engineering with Shanghai Jiao Tong University. His current research interests include SLAM and computer vision, in particular, 2D-3D registration and camera localization.



**Yu Zheng** is currently pursuing the B.Eng degree in Department of Artificial Intelligence, Shanghai Jiao Tong University. His latest research interests include SLAM and computer vision.



**Yanfeng Guo** received his B.Eng degree at Department of Automation from Shanghai Jiao Tong University, Shanghai, China, in 2022. He is currently pursuing the M.S degree in Electrical and Computer Engineering at University of California, Los Angeles, the United States. His current research interests include computer vision and autonomous driving system.



**Zhe Liu** received his B.S. degree in Automation from Tianjin University, Tianjin, China, in 2010, and Ph.D. degree in Control Technology and Control Engineering from Shanghai Jiao Tong University, Shanghai, China, in 2016. From 2017 to 2020, he was a Post-Doctoral Fellow with the Department of Mechanical and Automation Engineering, The Chinese University of Hong Kong, Hong Kong. From 2020 to 2022, he was a Research Associate of Department of Computer Science and Technology, University of Cambridge, United Kingdom. He is currently a tenure-track associate professor of Institute of Artificial Intelligence, Shanghai Jiao Tong University. His research interests include scheduling and optimization of large-scale robotic systems, resilient navigation of industrial self-driving systems, localization of self-driving systems, coordination of multi-robot formations, and robot control.



**Yixiang Zhu** is currently pursuing the B.Eng degree in Department of Electrical Engineering, Shanghai Jiao Tong University. His latest research interests include SLAM and computer vision.



**Wolfram Burgard** is Vice President for Automated Driving Technology at the Toyota Research Institute in Los Altos, USA. He is on leave from a Professorship for Computer Science at the University of Freiburg, Germany where he heads the Laboratory for Autonomous Intelligent Systems. He received his Ph.D. degree in computer science from the University of Bonn in 1991. His areas of interest lie in robotics and artificial intelligence. In the past, Wolfram Burgard and his group developed several innovative probabilistic techniques for robot navigation and control. They cover different aspects including localization, mapping, path planning, and exploration. For his work, Wolfram Burgard received several best paper awards from outstanding national and international conferences. In 2009, Wolfram Burgard received the Gottfried Wilhelm Leibniz Prize, the most prestigious German research award. In 2010 he received the Advanced Grant of the European Research Council. Wolfram Burgard is the spokesperson of the Cluster of Excellence BrainLinks-BrainTools, President of the IEEE Robotics and Automation Society, and fellow of the AAAI, EurAI and IEEE.



**Hesheng Wang** received the B.Eng. degree in electrical engineering from the Harbin Institute of Technology, Harbin, China, in 2002, and the M.Phil. and Ph.D. degrees in automation and computer-aided engineering from The Chinese University of Hong Kong, Hong Kong, in 2004 and 2007, respectively. He is currently a Professor with the Department of Automation, Shanghai Jiao Tong University, Shanghai, China. His current research interests include visual servoing, service robot, computer vision, and autonomous driving. Dr. Wang is an Associate Editor of IEEE Transactions on Automation Science and Engineering, IEEE Robotics and Automation Letters, Assembly Automation and the International Journal of Humanoid Robotics, a Technical Editor of the IEEE/ASME Transactions on Mechatronics, an Editor of Conference Editorial Board (CEB) of IEEE Robotics and Automation Society. He served as an Associate Editor of the IEEE Transactions on Robotics from 2015 to 2019. He was the General Chair of IEEE ROBOT 2022 and IEEE RCAR 2016, and the Program Chair of the IEEE ROBOT 2014 and IEEE/ASME AIM 2019. He will be the General Chair of IEEE/RSJ IROS 2025.